TRIBOMETER-BASED QUANTIFYING OF FRICTION IN METAL CUTTING

TRIBOMETER-BASED QUANTIFYING OF FRICTION IN METAL CUTTING

By

JEREMY BOYD, B. Eng.

(McMaster University, Canada)

A Thesis

Submitted to the School of Graduate Studies

in Partial Fulfilment of the Requirements

for the Degree

Master of Applied Science

McMaster University

MASTER OF APPLIED SCIENCE (2012)   McMaster University

(Mechanical Engineering)   Hamilton, Ontario

TITLE: Tribometer-Based Quantifying of Friction in Metal Cutting

AUTHOR: Jeremy Boyd, B. Eng. (McMaster University, Canada)

SUPERVISOR: Dr. Stephen Veldhuis

                    Department of Mechanical Engineering

                    McMaster University

NUMBER OF PAGES: x, 89

Abstract

The objective of this research was the further development and characterization of a heavy load, high temperature pin on disc tribometer. The goal of performing this testing on the tribometer is to simulate realistic machining conditions experienced between a tool and workpiece 'offline' in order to reduce the number of real machining trials used to select a tool coating and subsequently optimize cutting parameters. This approach is based on the understanding that a change in the cutting speed can alter the tool-chip interface temperature profile, which can change the coefficient of friction (COF) between the tool and workpiece and impact the tool wear mechanisms and rate.

Significant modifications were introduced to the tribometer to increase its functionality; a resistance welder was integrated into the setup, and a completely new, fully automated Graphical User Interface was designed using National Instruments Labview software to allow for more careful control of all interacting components and variables. Careful investigations were carried out to understand the sensitivity of COF measurements to various input parameters in order to gain increased confidence in the meaning of COF measurements. Finally, various tool and workpiece material pairs were tested from room temperature to upwards of 900°C near the pin-disc interface and efforts were made to correlate the resulting COF measurements with machining data in the form of tool life and cutting force measurement.

This research contributes towards the goals of improving machinability in two ways: first, by screening potential surface engineering treatments on the basis of reduced friction under machining relevant conditions of elevated contact stress and temperature;

and secondly, by generating temperature-dependent friction data for different tool and workpiece material pairs that can be used to improve FE simulations of metal cutting.

Acknowledgements

I would first like to thank my thesis supervisor, Dr. Veldhuis, for entrusting me with a challenging research project and supporting me throughout this two-year journey. Thanks for painting a big picture to help keep me on track while bearing patiently with my detail-oriented approach. Thanks as well for all of your suggestions that have helped make this work a success and for your financial backing.

Thanks to Andrew Biksa for your mentorship as I began to work and experiment with the tribometer and for offering valuable feedback on my thesis. Similarly, thanks to Mohammed Tauhiduzzaman for giving it a very thorough review and thanks to Dr. Ng and Dr. Koshy for sitting on my Thesis Defence Committee and providing a very constructive critique of my thoughts and research.

Thanks to my many colleagues in the MMRI for your suggestions and assistance in my work; notably Terry Wagg, Steve Remilli, Maneesh Khanna, Manuel Abad, Kevin Tenaka, Mark Dubois, Simon Oomen-Hurst, William Long and Hao Yu Li. Special thanks to Dr. Fox-Rabinovich for the many invaluable discussions on tool wear and coatings in machining. Also, a special thanks to Joe Verhaeghe from the 2nd floor shop for his assistance with anything electrical or electronic in nature.

Thanks to my wife, Karen, for your tireless emotional support and deep well of love that helped spur me on to completing this thesis, and for helping to bring some balance to my work-driven personality.

Lastly, thanks to Jesus Christ, for loving me, giving up your life for me on the cross, and never letting go of me.

Table of Contents

List of Figures

List of Tables

Declaration of Academic Achievement

The contributions of the author to this thesis are as follows: the acquisition, testing and integration of an electrical resistance welder into the tribometer setup and the necessary mechanical changes to the tribometer to permit such integration; the design of a Graphical User Interface using National Instruments Labview software to perform control of actuators and measurement of critical variables; the various investigations carried out on the tribometer to explore the effect of input parameters (notably the magnitude of the applied normal load and the length of time of rotation) on the output parameters (notably the normal contact stress, the friction coefficient and the maximum achievable interface temperature); and the generation of COF vs. Temperature data for various tool and workpiece material combinations.

The author would like to acknowledge Dr. Peidong Wu for proposing the mechanism of von Mises stress criteria by which the imprint tends to grow in size once rotation has begun.

The author would like to acknowledge the FE simulation work of Hao Yu Li used to generate an estimate of true interface temperate data versus imprint diameter, which was used to draw conclusions regarding the differences in induction heating versus resistance heating methods.

Chapter 1. Introduction

Metal-cutting, often referred to as machining, is an important manufacturing process used by the automotive, aerospace, rail and many other industries. It is a process of material removal, whereby a sharp tool moving relative to a workpiece successively shears a thin layer of material from the bulk, which then flows over the face of the tool in the form of a 'chip' and eventually separates. From a mechanical point of view, the cutting edge of the tool is subject to very demanding conditions, with contact stresses approaching three times the room temperature hardness of the workpiece and temperatures often exceeding 1000°C.

In general, a faster rate of material removal is desirable from a production standpoint, and high speed machining can be economically advantageous in terms of power consumption as the cutting forces tend to drop as cutting speed is increased. However, the speed of machining is often limited by the machine tool itself (spindle power, machine dynamics) and the rate at which the cutting edge of the tool wears.

Assuming the machine tool itself is adequate for the task, the limiting factor becomes the wear rate of the tool and its effect of increasing the machining power required or compromising the dimensional accuracy and surface quality of the resulting component. 'Tool life' can be measured in terms of number of components/features machined or the total length of cut or total time of cut before a tool needs to be replaced for one of the aforementioned reasons. Alternatively, ANSI/ASME B94.55M-1985 established the criteria of 0.3 mm average flank wear or 0.6 mm maximum flank wear (for an irregularly worn tool flank face) as a standardized limit of tool wear, after which the tool should be

replaced or reground (American National Standard, 1985). For a given workpiece, increasing the cutting speed generally leads to a decrease in tool life and more frequent replacement of tools, which is a low value-added task.

Thus, an active area of research in machining is the development of improved tool materials that can better withstand the various forms and mechanisms of wear experienced during machining, leading to increased tool life as well as higher cutting speeds. The application of hard coatings to the surface of the tool substrate through processes such as Physical Vapour Deposition is one such approach. However, quantifying the effectiveness of a coating in increasing tool life typically involves machining a large quantity of expensive workpiece material; furthermore, such conventional tool wear testing does not provide any information regarding the contact conditions at the tool-chip interface that govern tool wear.

Within the McMaster Manufacturing Research Institute (MMRI), there is a move towards a more physics-based approach for selecting and even designing coatings and surface engineering treatments for cutting tools. Part of this involves Finite Element modeling of the machining process under the cutting speed, feed rate and depth of cut of interest in order to get an estimate of the normal stress and temperature distribution on the cutting tool. This involves rather detailed knowledge of tool and workpiece material behaviour at elevated temperatures and high rates of strain and strain rate, which is available in the form of Johnson-Cook parameters for various materials of interest. A common challenge, however, is that of accurately quantifying and modeling friction at the chip-tool interface (Filice, Micari, Rizzuti & Umbrello, 2007).

Another aspect of this physics-based approach is to subject the tool substrate and coating to bench-scale test equipment used to simulate different conditions and phenomena that occur in machining operations. One such instrument is a heavy load, high temperature tribometer developed by a former graduate student, Andrew Biksa. With it, Biksa attempted to quantify the adhesive interactions between tool-workpiece material pairs as a coefficient of friction under machining-like conditions of elevated contact stress and temperature.

This present thesis builds off Biksa's work by adding increased functionality to the tribometer. Specifically, a resistance welder was purchased and carefully integrated into the experimental setup in an effort to increase the achievable pin-disc interface temperatures and generate temperature gradients more representative of machining. Additionally, much work went into designing a new Graphical User Interface (GUI) in Labview that would incorporate increased safety, easier operation, and improved repeatability as well as greater flexibility in test procedures. As well, an extensive exploration on the sensitivity of friction coefficient measurements to numerous input variables was conducted in order to gain improved confidence in the accuracy and meaning of the friction measurements. Lastly, tribometer tests involving various tool and workpiece material combinations were conducted, as were machining tests involving tool wear and tool force measurement. Discussion of these results focuses on how the tribometer can be used as a practical aid to the challenge of selecting a coating for improved tool life as well as in modeling tool-chip friction in Finite Element metal cutting models.

Chapter 2. Literature Review

The following literature review provides a brief background on some topics related to the content of this thesis, namely friction and surface interactions; friction in metal cutting; tool wear and the role of coatings; and some experimental tribometers developed by other researchers for the purpose of characterizing friction in metal cutting applications.

2.1 Friction and Surface Interactions

Friction is the resistance to tangential motion between two surfaces under a normal load. Referring to Figure 1, if a force F_A is applied in the direction of motion to a body moving at constant velocity, an equal but opposite friction force F_f will resist this motion. Common observations are that the ratio of this friction force F_f to the normal force F_N is independent of the normal force as well as the apparent area of contact between the two surfaces. Mathematically, this is expressed as in equation 2.1, where μ is referred to as the coefficient of friction:

$$\mu = \frac{F_f}{F_N}$$
Equation 2.1
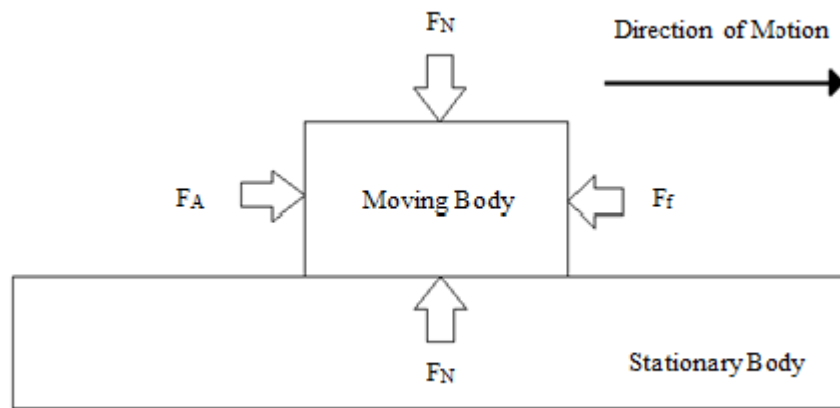
Figure 1: Free body diagram of sliding body experiencing friction

Rabinowicz (1995, p. 78) estimates that as much as 90% of the friction force can be accounted for by the need to shear adhesive bonds formed between atoms at the contacting surfaces, the balance being attributed to roughness, the mechanical interlocking of surface asperities, as well as ploughing and electrical effects. Strictly speaking, adhesion is the phenomena observed whereby after pressing two surfaces together under some normal compressive load, possibly but not necessarily combined with some shear load, a normal tensile force is required to separate those two surfaces. Adhesion can be quantified in terms of a coefficient of adhesion, defined as the ratio of the normal tensile load $F_N{}'$ required to separate the surfaces to the normal compressive load F_N initially applied, or f':

$$f' = \frac{F_N{}'}{F_N} \qquad\qquad \text{Equation 2.2}$$

Rabinowicz (1995, p. 267) suggests that the seemingly seldom occurrence of adhesion between surfaces can be attributed to three phenomena: the relatively small *real* area of contact between most surfaces (as will be subsequently discussed); the abundant presence

of contaminants and oxide layers on most surfaces; and the tendency for elastic residual stresses to break adhesive joints upon unloading. He notes as well that the application of shear forces and sliding between two surfaces tends to increase adhesion by increasing the *real* area of contact and by enabling surface oxide and contaminant layers to be broken up such that metal-to-metal contact can be established (Rabinowicz, p. 280).

As alluded to earlier, when two surfaces are brought together under a normal load, that load is not uniformly carried over the entire apparent contact area but rather by the area made up of contacting surface asperities, as illustrated in Figure 2. Strong atom-to-atom forces are influential only over a very short length scale, on the order of a few Angstroms (Rabinowicz, 1995, p. 44), so it is the *real* area of contact A_r, the summation of the area of these contacting asperities or junctions, that governs the magnitude of the friction force between two surfaces, not the *apparent* area of contact A_a viewed macroscopically.

$$Real\ Area,\ A_r = A_1 + A_2 + A_3 + \ldots + A_N$$
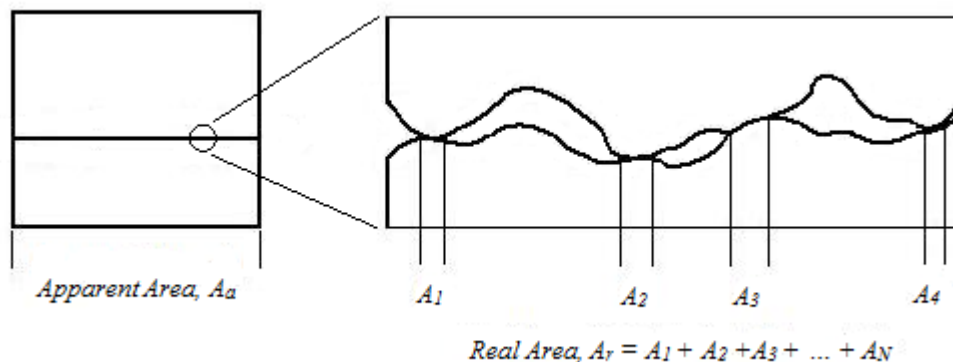
Figure 2: Illustration of apparent versus real area of contact between two surfaces

Upon contacting, these surface asperities deform elastically at first, and then plastically if necessary, until the sum of the product of contact stress and contact area at each pair of surface asperities can balance the applied normal load. As this normal load is increased, new junctions will form and grow in size as well, thus the real area of contact will continue to grow as the applied load is increased. Under purely normal load, Rabinowicz proposes that the real area of contact A_r can be no less than, and in many cases is thought to be very close to, the ratio of the normal load F_N to the brinell hardness of the softer material p (1995, p. 45):

$$A_r \geq \frac{F_N}{p} \qquad\qquad \text{Equation 2.3}$$

However, the addition of shear forces acting on the junctions can lead to a considerable increase in the real area of contact, having increased nearly threefold at the onset of sliding (Rabinowicz, 1995, p. 47).

In order for relative sliding motion between two bodies to occur, these junctions must be broken and subsequently reformed. Assuming an average junction shear strength, the total friction force can be expressed as:

$$F_f = \tau_{av} \cdot A_r \qquad\qquad \text{Equation 2.4}$$

From Equations 2.1, 2.3 and 2.4 the friction coefficient can be expressed as:

$$\mu = \frac{F_f}{F_N} = \frac{\tau_{av} \cdot A_r}{p \cdot A_r} = \frac{\tau_{av}}{p} \qquad\qquad \text{Equation 2.5}$$

Rabinowicz (1995, p. 75) proposes that the average junction shear strength is approximately equal to the shear strength of the softer of the contacting materials; indeed, if it were considerably higher, the tendency would be for the junction to consistently

shear within the softer material, resulting in a particle of the softer material adhering to the surface of the harder material. However, this occurs at only 1 to 10% of the rate of the formation and break-up of junctions between uncontaminated metal surfaces in an air environment (Rabinowicz, 1995, p. 75). Similarly, if the average shear strength at the junctions was much lower than the shear strength of the softer material, one would anticipate consistently clean shearing at the interface between the two materials without the transfer of softer material to the harder material that is commonly observed.

Shaw (1984, p. 202) makes an important distinction in the field of friction between what he refers to as lightly loaded sliders and heavily loaded sliders. As the applied load between two surfaces increases, plastic deformation is no longer constrained to the contacting asperities resulting in their further flattening. Rather, the subsurface will begin to flow plastically, the transition of which begins around $A_r/A_a = 1/3$. Growth in the *real* area of contact and the associated rise in friction force continues as applied load increases, but at a reduced rate. Shaw, Ber, and Mamin (1960) constructed an experimental apparatus to explore the frictional behaviour of materials under heavily loaded sliding conditions. It involved loading a hard steel ball against a soft steel surface until plastic flow occurred. Measurement of the torque required to slide the soft steel specimen relative to the ball at low speeds, combined with measurement of the applied load and the projected area of contact after the test, enabled the estimation of the mean normal stress and shear stress. Variation of the normal load enabled the generation of different mean normal stresses. The results of their tests, qualitatively reproduced in Figure 3, illustrate the variation of the coefficient of friction with changing normal stress,

σ, which they link to the ratio of real and apparent areas of contact, A_r/A_a. Region I is where classical laws of sliding friction apply. Region III represents conditions of shear within the bulk of the softer material. Region II represents a transition between Regions I and III in which subsurface plastic flow occurs in parallel to surface sliding, and which the authors claim is representative of tool-workpiece interactions in metal-cutting and forming operations (Shaw et al., 1960).
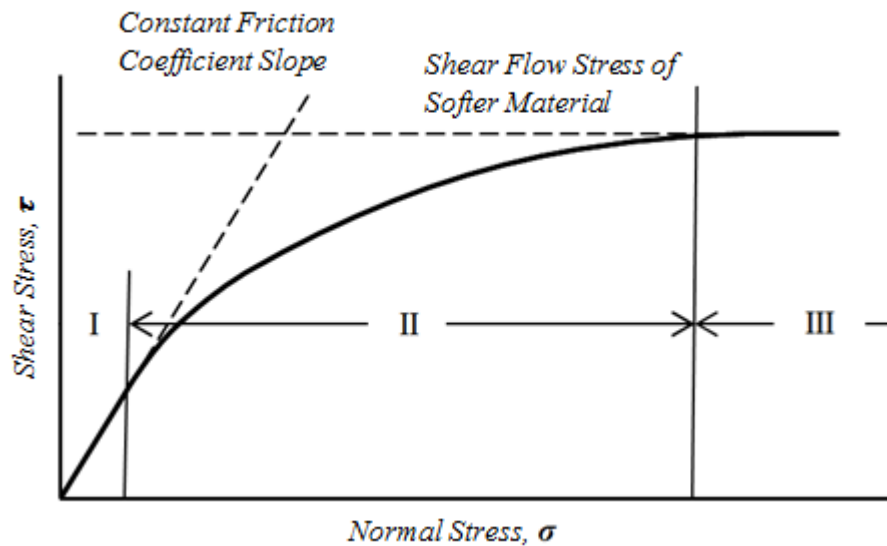
Figure 3: Variation of Shear Stress with Normal Stress (adapted from Shaw et al., 1960)

2.2 Friction in Metal Cutting

Metal cutting is a process of material removal whereby a tool engages a workpiece in relative motion, successively fracturing and shearing material from the workpiece in the 'primary shear zone'. The result is the formation of the 'chip', which flows over the rake face of the cutting tool, and the machined surface, which is formed after rubbing against portions of the cutting edge radius and the flank face of the tool.

One of the earliest models to explain the mechanics of metal cutting was set forth by Merchant (1945), who assumed that shearing of the workpiece was largely contained within a plane inclined at an angle φ to the resulting workpiece surface, as depicted in Figure 4. Merchant also assumed that the resulting chip slides over the rake face of the cutting tool under a constant friction coefficient. Experimental measurement of the cutting force F_c and thrust force F_t, combined with knowledge of the tool rake angle α, enables the calculation of this friction coefficient according to Equation 2.6, derived from Merchant's model.

$$\mu = \frac{F}{N} = \frac{F_c \sin \alpha + F_t \cos \alpha}{F_c \cos \alpha + F_t \sin \alpha} \qquad\qquad \text{Equation 2.6}$$
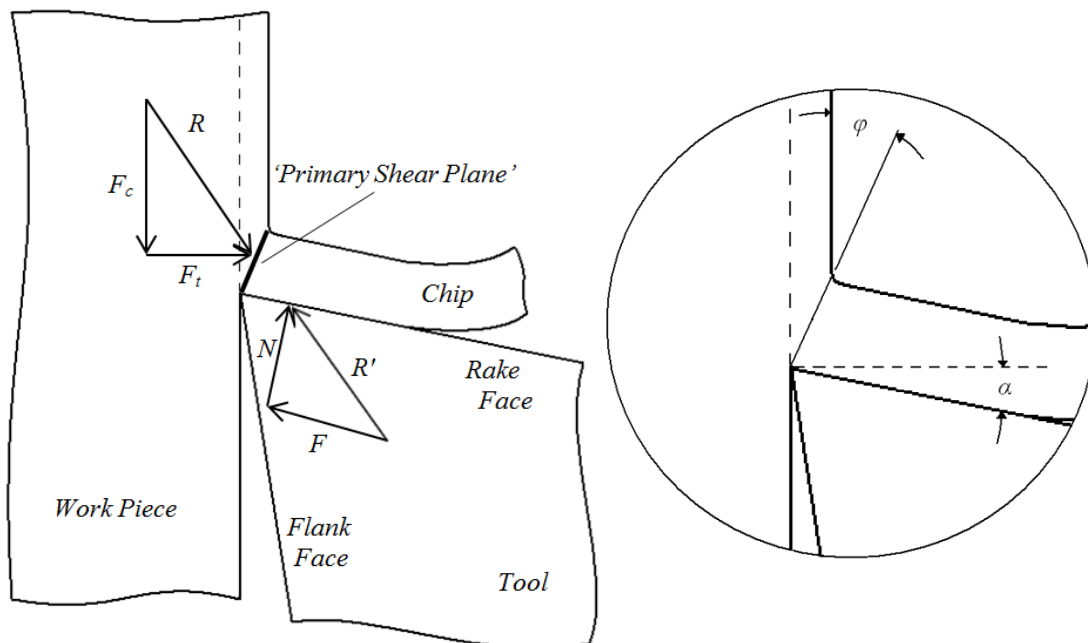
Figure 4: Schematic of Metal Cutting Mechanics and Geometries

However, subsequent work reported by many researchers, including Zorev (as cited in Shaw, 1984), has demonstrated that the local friction coefficient at the tool-chip interface is not at all constant but varies substantially over the tool-chip contact length, l_c. Roughly speaking, the tool-chip interface can be divided into two regions, a sticking region and a sliding region, as shown schematically in Figure 5. Normal contact stress σ is at its maximum near the cutting edge and decays in a roughly parabolic manner toward the end of the tool-chip contact length. Shear stress τ is essentially constant and equal to the workpiece material shear flow stress k over the first half of the tool-chip contact length, near to the cutting edge; it then decays proportionally with normal stress toward the end of the tool-chip contact length. Mathematically, this can be modeled as follows (Filice et al., 2007):

$$\tau = k, \qquad 0 < x < l_c/2$$

$$\tau = \mu_{sl} \cdot \sigma(x), \; l_c/2 < x < l_c$$

Equation 2.7
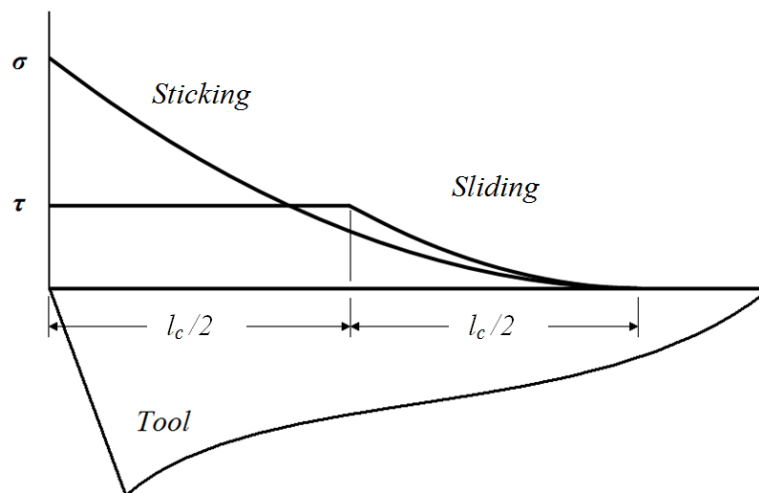
Figure 5: Sticking and Sliding at the Tool-Chip Interface

Bailey (1975) points out that when sticking friction is present, the variation of mean friction coefficient with changing cutting speed may be due to changes in mean normal stresses, mean shear stresses or both. It follows that a reduced mean friction coefficient may not reflect actual reduced sticking or adhesion of the chip to the tool.

Trent made significant contributions to explaining the cause of the sticking region in the tool-chip interface, linking it to seizure or cold-welding of the freshly generated, chemically active surface of the chip to the tool rake face under extreme normal stress and elevated temperatures (1988a). Under conditions of seizure, the velocity profile of the chip tends to zero as the seized layer is approached, resulting in additional and substantial plastic deformation. At lower cutting speeds, the result is the formation of successively adhered layers of severely strain hardened chip material, referred to as a built-up-edge (BUE). At higher cutting speeds and feeds, which trigger elevated temperatures (Trent, 1988c), thermal softening will dominate strain hardening tendencies within the chip material. This results in a transition from BUE formation to that of a thin secondary shear zone, also known as a 'flow zone', which typically ranges between 10 to 80μm in thickness (Trent, 1988a). For the reader's reference, these two different manifestations of seizure are illustrated in Figure 6. Trent (1988b) notes that this flow zone is typically more strongly adhered to the tool than is the BUE; he also comments that the behaviour of metals and alloys within the flow zone can be likened to very viscous liquids, exhibiting virtually unlimited deformation at constant or decaying yield strength.
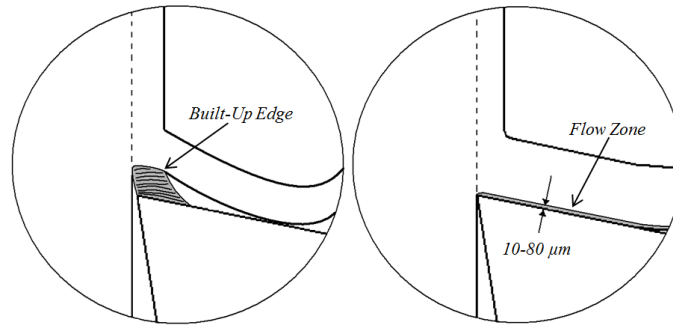
Figure 6: Manifestations of Seizure as a Built-Up Edge or Flow Zone

In light of these observations, he states: "Under conditions of seizure there is no significant relationship of frictional to normal force corresponding to the coefficient of friction (Trent, 1988b)." However, Trent does acknowledge the presence of sliding contact conditions around the peripheral of the tool-chip contact region, where contact stresses must naturally be lower and the surrounding atmosphere is able to penetrate the interface; he notes a wavy, segmented nature to the edges of chips characteristic of the stick-slip phenomenon (Trent, 1998b).

Since Merchant's initial sliding friction model and Zorev's observation of sticking and sliding regions, researchers in metal cutting have proposed other friction models as well. Filice et al. (2007) highlight a few different models. In addition to those of Merchant as well as Zorev is a constant shear stress model, in which the interfacial shear stress, τ, between tool and chip is assumed to be a constant fraction, m, of the shear flow stress of the workpiece material, k, along the entire tool-chip contact length.

$$\tau = m \cdot k \qquad \text{Equation 2.8}$$

Another is an empirical equation proposed by Usui and Shirakashi.

$$\tau = k\left[1 - e^{-(\mu \cdot \sigma / k)}\right] \hspace{3cm} \text{Equation 2.9}$$

Similar is that proposed by Childs, who modifies the model by multiplying the material shear flow stress, *k*, with a fractional friction factor, *m*, and introducing an exponential term *n*.

$$\tau = m \cdot k\left[1 - e^{-\left(\frac{\mu \cdot \sigma}{m \cdot k}\right)^n}\right]^{\frac{1}{n}} \hspace{2cm} \text{Equation 2.10}$$
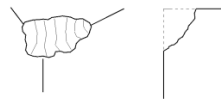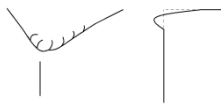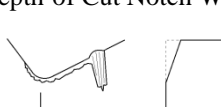
Filice et al. (2007) conducted orthogonal cutting tests of AISI 1045 steel using an uncoated cemented carbide insert and experimentally measured tool forces, tool-chip contact length, chip thickness and shear angle. Finite Element metal cutting simulations under the same conditions were then run using each of the different friction models, tuning their parameters as necessary in an effort to match model predicted outputs with those experimentally measured. Each of the friction models led to quantitatively similar results; the cutting force was accurately predicted, while the other outputs were notably different from experimental values. This author must readily admit his inexperience in the field of FE modeling, but the results of Filice et al. (2007) would suggest that the poor predictive performance of FE models to date are primarily due either to other poorly modeled aspects of machining (i.e. the friction model does not matter) or to inadequacies of the proposed friction models, which likely overlook key phenomena responsible for friction.

2.3 Tool Wear and the Role of Coatings

The purpose of a cutting tool in a machining operation is the controlled removal of workpiece material in order to produce a surface of desired quality in terms of dimensional accuracy, surface finish (roughness) and residual stress. The geometry and material of the tool as well as the specific cutting parameters (cutting speed, feed rate, and depth of cut) all play an important role to this extent. Ideally, the tool would maintain its geometry indefinitely; in reality, however, the thermal, mechanical and chemical interactions between the cutting tool and the workpiece lead to various forms of tool wear, changing the geometry of the tool close to the cutting edge. This in turn tends to increase the cutting forces and power consumed in a machining process as well as compromise the quality of the surface produced. At a certain point, the tool is no longer economically viable for use and must be either reground or replaced, both of which trigger low value-added manual labour in a process. Thus, the ability of a cutting tool to resist the various forms and mechanisms of wear is of great economic interest. In reality, many of these wear mechanisms will act in parallel, although one is usually more dominant than others and limits the usable life of the tool for the given workpiece material and cutting parameters. Typical forms of tool wear, as well as their underlying mechanisms and negative impact on machining, are summarized in Table 1.

An important class of cutting tool materials employed today is that of cemented tungsten carbides. There are actually two different tungsten-based carbides – WC decomposes at 2600°C, while W_2C melts at 2750°C (Trent & Wright, 2000, p.175). However, it is WC that has been more dominantly used in tooling materials. Tools are

Table 1: Summary of tool wear forms, mechanisms and their impact on machining (SANDVIK, 1996)

Form of Tool Wear or Failure	Underlying Mechanism(s)	Impact on Machining
Gross Tool Edge Fracture		Major increase in tool forces and cutting power required; very poor surface roughness; loss of dimensional accuracy; increased surface roughness; loss of dimensional accuracy
Tool Edge Deformation	Plastic deformation (owing to excessive temperatures and contact stresses)	Poor chip control; poor surface roughness; risk of gross tool edge fracture for brittle tool materials
Tool Edge Chipping	Adhesion; fatigue (cyclic thermal loading)	Increased tool forces; poor surface roughness
Built-up Edge (BUE)	Adhesion	Loss of dimensional accuracy; risk of tool edge chipping
Flank Wear	Abrasion (to a lesser extent, adhesion and diffusion)	Increased tool forces; poor surface roughness; induces residual tensile stresses in machined surface
Crater Wear	Diffusion	Weakens tool edge, increasing risk of deformation and gross fracture
Depth-of Cut Notch Wear	Oxidation and/or abrasion	Poor surface finish; weakens tool edge, increasing risk of deformation and gross fracture
Thermal Cracking	Cyclic thermal loading	Poor surface finish; leads to edge chipping

16

typically made by pressing a fine powder mixture of WC and cobalt into a compact and then sintering it through heating in hydrogen above 1300°C (Trent & Wright, 2000, p. 176). For cutting tools, the size of carbide grains can vary from 0.5 to 10 μm and the typical range of cobalt content is 3 to 12 percent, where an increase in cobalt content leads to increased fracture toughness accompanied by reduced hardness. These WC-Co alloys are classified as K-type carbides under ISO designation and are applicable for the machining of cast irons and non-ferrous metals. Some of the WC content can be replaced by harder and more decomposition-resistant carbides. These (WC+TiC+TaC)-Co alloys are classified as P-type carbides under ISO designation and are typically used in the machining of steels, exhibiting enhanced resistance to crater wear on the tool rake face. However, the balance of discussion on cemented carbides will focus on the K-type designation (WC-Co) as this corresponds to the grade used by Biksa (2010) and the present author.

Table 1 presented a wide variety of tool wear forms and the underlying mechanisms that cause them. Some of these mechanisms and the ability of WC-Co to resist them will now be briefly discussed.

Plastic deformation: the machining of hard materials under aggressive chip loads can trigger sufficiently high temperatures to soften the tool material; the associated contact stresses are then able to cause plastic deformation of the tool edge and nose (Trent & Wright, 2000, p. 186). As mentioned earlier, reducing the cobalt content will generally lead to increased hardness, and thus increased resistance to plastic deformation.

Diffusion wear: especially when machining steels at high speeds and feeds, a crater is commonly formed on the rake face of the tool. This is typically linked to the diffusion of metal and carbon atoms from the tool material into the seized material in the chip flow zone (Trent & Wright, 2000, p. 189). Diffusion is extremely sensitive to temperature; an increase of only 10°C can increase diffusion rates by a factor of 2 or 3 (Taminiau & Dautzenberg, 2003, p. 12). Diffusion also increases with a more rapid flow rate in the workpiece material, thus it can be a contributing mechanism for wear at the flank face on account of the more rapid material flow relative to the rake face; at higher cutting speeds it can even be considered the dominant mechanism of flank wear (Trent & Wright, 2000, p. 157, 195).

Adhesive wear: at lower cutting speeds, seizure of the chip to the tool typically manifests as a built-up edge (BUE). As discussed earlier, a BUE is inherently unstable in nature and prone to breaking off; if the layers are sufficiently strain hardened and the BUE is firmly seized to the tool substrate, the entire BUE and some portion of the tool edge may be torn away. Trent and Wright remark that a WC-Co tool's resistance to attrition wear is primarily linked to grain size, finer-grained carbides exhibiting improved resistance, whereas the cobalt content shows very little influence (2000, p. 198).

Abrasive wear: hard inclusions in the workpiece can potentially plough through comparably softer WC grains and the cobalt binding matrix in WC tooling. For instance, WC has a hardness of about 2100 HV, whereas TiC is about 3200 HV and V_4C_3 is around 2500 HV (Trent & Wright, 2000, p. 177). Nonetheless, it is doubtful that such hard inclusions would succeed in ploughing through even the cobalt matrix under conditions of

seizure, though they may have more success in regions where sliding occurs (Trent & Wright, 2000, p. 200). Reducing the cobalt content as well as carbide grain size increases the hardness of the alloy, which has been shown to be directly proportional to the abrasive wear resistance of a material (Rabinowicz, 1995, p. 194).

Oxidation wear: very often, accelerated wear in the form of deep grooves or notches occurs at peripheral regions of contact between the tool, chip and workpiece surface (Trent & Wright, 2000, p. 202). In these peripheral regions, the normal contact stress is greatly reduced; the real area of contact is considerably less than the apparent area of contact; relative motion is governed by sliding or a 'stick-slip' phenomenon as opposed to complete seizure; and the surrounding atmosphere can penetrate the interface and react with the chemically active surfaces of the chip and tool. Whittle and Stringer (1980) suggest that alloys which successfully withstand degradation under high temperature oxidation must form surface oxides that (1) thicken at a relatively slow rate and (2) adhere well to the alloy surface under the conditions of exposure. Unfortunately, both tungsten and cobalt form very porous oxides that can be easily removed by the chip under sliding conditions (SANDVIK, 1996, p. IV-7). Sheikh-Ahmad and Bailey (1999) suggest that abrasion works in conjunction with oxidation to produce macroscopic wear, the hard alloying elements in the chip ploughing through brittle, rutile oxides formed on the tool surface.

As already alluded to, resistance to some of the aforementioned wear mechanisms can be improved by reducing the grain size and cobalt content of the WC-Co alloy, at the risk of making the tool excessively brittle and prone to gross tool edge fracture. However, a

different approach must be taken to improve resistance to diffusion and oxidation wear, both of which are very chemical and temperature dependent in nature. This leads us to the topic of surface protecting coatings.

Coatings were first applied to cutting tools in the late 1960's, the driving impetus being the reduction of crater wear in steel-cutting grade carbide tools (Shaw, 1984, p. 351). Today, upwards of 80% of all carbide tools used in machining are coated in some manner (Biksa, 2010, p. 77). These coatings range in chemical composition, microstructure and architecture, thickness, and method of application. Most commercially available coatings today belong to the family of TiN coatings, additional alloying elements including but not limited to Al, Cr, C, Y and Si. Common methods of depositing the coating to the tooling substrate include Chemical Vapour Deposition (CVD) and Physical Vapour Deposition (PVD). The latter type of coatings are deposited at lower temperatures (300-600°C) and under increased vacuum conditions (10^{-4} mbar) than are CVD coatings; they also tend not to exceed 5 μm thickness, whereas coatings deposited by CVD can reach up to 20 μm (Prengel, Pfouts & Santhanam, 1998).

The benefit to proper coating selection and application is an increased resistance to the various wear mechanisms previously discussed, enabling a combination of longer tool life and increased metal removal rates. However, inadequate adhesion between the coating and the substrate can lead to coating failure by delamination, thereby exposing the underlying substrate to the same aggressive mechanisms. Prengel et al. (1998) note that interdiffusion of coating and substrate atoms during the nucleation stage of coating

deposition helps to promote good coating adhesion, as does the overall cleanliness of the substrate surface prior to deposition.

The relatively low thermal conductivity of many coating materials relative to WC-Co led to the thought that coatings thermally insulate the tool, reducing the heat input and temperatures within the substrate material. However, various Finite Element simulations would suggest this is not the case. Klocke and Kriege (1999) discuss how a coating with low thermal conductivity and a low heat transmission coefficient at the coating-substrate interface leads to higher temperatures within the coating itself but no appreciable change in the thermal gradients or delay in the increase of heat within the body of the substrate. Rech, Battaglia and Moisan (2005) showed that the thermophysical properties and thickness of a coating only noticeably affect the thermal behaviour of the coated tool during small durations of contact between the tool and chip ($< 10^{-2}$ s); they thus suggested that coatings can provide beneficial thermal protection in high speed interrupted machining processes but not in continuous machining operations such as turning. However, it stands to reason that a coating can still lead to reduced temperatures in the tool substrate if the rate of heat generation at the tool-chip interface were reduced due to improved tribological conditions.

Notwithstanding the importance of bulk properties of the coating, such as hot hardness and oxidation resistance, the nature of tribofilms that form on the coating surface as a result of aggressive friction between tool and chip has been recognized as of paramount importance. Beneficial tribofilms are either lubricious in nature or of sufficient chemical stability that they tend to reduce sticking and seizure of material to the tool rake

face. The formation of aluminum oxide (Al_2O_3) on the surface of TiAlN coatings is a

prime example (Klocke & Kriege, 1999; Fox-Rabinovich et al., 2010).

2.4 Machining-Relevant Tribometers

It is noteworthy that the MMRI is not the only research group with an interest in

quantifying friction between tool and workpiece materials in metal cutting applications. A

few of the more recent tribometers developed to this end as found in literature as well as

that developed by Biksa are briefly described here for the purpose of comparison and to

highlight areas for improvement.

A research group from Ecole Nationale d'Ingénieurs de Saint Etienne (ENISE) has

developed a few iterations of a tribometer they claim to be suitable for simulating the

conditions present in machining. The first iteration (Zemzemi, Ben Salem, Rech, Dogui &

Kapsa, 2008) involves a tubular workpiece gripped in the chuck of a lathe. A spherical tip

cemented carbide pin is loaded against the face of the tube by a pneumatic jack.

Diametrically opposed, a cutting insert refreshes the contact surface as the tube is rotated.

A feed per revolution of 0.3 mm/rev is employed to ensure that the plastically affected

layer in the workpiece resulting from loading of the pin is fully removed. The pins are

held in a special holder that enables quantification of heat flux into the pin through

special methods developed by the authors. The pin holder itself is fixed onto a

dynamometer such that normal and tangential forces can be measured and an apparent

friction coefficient calculated as the ratio of tangential and normal force. A variety of pin

diameters and applied loads allows for reasonable variation of contact stresses in the

range of 1 to 3 GPa, and sliding speeds between the pin and workpiece can reach as high as 16 m/s. Furthermore, the pin is continually interacting with new workpiece material – thus the setup can be considered an 'open' tribosystem, similar to metal cutting itself. Limitations observed, however, were the limited duration of the tests (< 10s), the labour involved in preparing the tubes, and the mechanical instability of the setup, which limited the practical range of sliding speeds and contact pressures.

Bonnet et al. (2008) introduced an improved configuration, which is the same as that used subsequently by Rech, Claudin and D'Eramo (2009). A cylindrical billet replaces the tube as the workpiece. The pin is now loaded radially against the cylindrical billet. Axial feeding of the pin combined with rotation of the workpiece leads to a helical path, the pin continually rubbing against new material. In between friction tests, the cylindrical billet surface is refreshed by a cutting tool and subsequently belt sanded to an average roughness of Ra~0.1 μm. The pins range from 9 mm to 17 mm in diameter with spherical geometry at their extremity and are polished to reach a low surface roughness of Ra < 0.3 μm.

For greater insight into the contact stresses and temperatures as well as local sliding speed, experimental work is followed up by numerical FE modeling of the pin on workpiece interaction. One of the primary aims is to isolate adhesive effects from ploughing effects in order to establish an adhesive friction coefficient. The authors neglect the coating in their model stating that its small thickness (5 μm) should have negligible effects on workpiece deformation and contact pressures; and citing previous investigations that demonstrated how the thermal insulation effect of such thin coatings is

negligible for long duration tests (> 0.1s). Modeling requires optimization or tuning of three different variables (indentation depth, adhesive friction coefficient, and heat partition coefficient) until the normal force, apparent friction coefficient and average heat flux transmitted to the pin from the model agreed with experimental findings within 5%.

The resulting output of investigations using these different configurations was an experimental coefficient of adhesive friction as a function of local sliding speed V_{ls} for a variety of tool and workpiece material pairs, as summarized in Table 2.

Table 2: Empirical functions relating friction coefficient to sliding speed found in literature

Tool vs. Workpiece Material	Empirical Relationship	Range of Applicability
TiN-coated WC-10Co vs. AISI 4142 steel	[a]$\mu_{adh} = -0.07 \cdot \ln(V_{ls}) + 0.57$	20 m/min $< V_{ls} <$ 170 m/min
TiN-coated WC-10Co vs. AISI 316L stainless steel	[b]$\mu_{adh} = -0.002V_{ls} + 0.39$	35 m/min $< V_{ls} <$ 90 m/min
TiN-coated WC-10Co vs. AISI 1045 steel	[c]$\mu_{adh} = -0.002V_{ls} + 0.498$	50 m/min $< V_{ls} <$ 103 m/min

[a] (Zemzemi et al., 2008)
[b] (Bonnet et al., 2008)
[c] (Rech et al., 2009)

The wide range of sliding speeds over which tests can be conducted and the elevated range of compressive stresses that can be achieved are definite strengths of the tribometers developed by the ENISE researchers, as is their achievement of an 'open' tribosystem. The lack of information regarding interfacial temperature, however, is a prominent limitation, as is the use of a dedicated industrial scale lathe. Furthermore, the requirement of FE simulation and extensive optimization in order to isolate the adhesive component of friction from a ploughing component is an additional drawback.

Another rather novel tribometer for measuring friction coefficient between tool-workpiece material pairs under contact conditions relevant to machining has been

developed by Puls, Klocke and Lung (2012), researchers at Aachen University in Germany. It is essentially a modified orthogonal cutting test set up on a lathe with a grooving tool held in a tool dynamometer, but the workpiece is rotated in the opposite direction such that the clearance face of the grooving tool becomes a highly negative angle rake face. Under feed rates $5 - 10$ times higher than those of conventional machining processes, the normal and shear stresses act on a simple inclined plane. A double light infrared pyrometer measures the temperature directly behind the tool. The setup effectively enables the measurement of friction coefficient under different forces, sliding velocities and temperatures. The duration of the test is less than one revolution to prevent the tool from rubbing against already deformed material; during the first 120° the tool plunges into the workpiece under constant feed rate, and forces and temperature gradually increases as the maximum deformed layer thickness is reached; during the next 120°, the tool is retracted at the same feed rate, and forces and temperature decrease. Furthermore, the process causes the enlargement of the disc width at the workpiece / tool interface; thus a considerable portion of the generated surface is actually virgin and chemically active, not having been exposed to the environment previously.

The authors tested uncoated cemented carbide tools (Sandvik H13A) against AISI 1045 steel in a normalized state. Surface speeds ranging from 20 to 200 m/min were employed, repeating each test 3 times. The friction coefficient was observed to be quite high at lower speeds (~ 0.6 at 20 and 50 m/min) and considerably lower at increased speeds (~0.31 at 100 m/min and ~0.23 at 200 m/min). It was observed that after a certain force and consequently a certain deformation had been reached during the test, the

friction coefficient was essentially constant, despite continuing increases in temperature. While the authors admitted that the measured temperature might be somewhat different from the interfacial temperature, these results led them to conclude that the friction coefficient was insensitive to temperature. This is different from the findings of Biksa and the general theory guiding the development of the MMRI tribometer, in which friction is believed to be temperature dependent. However, upon closer inspection of the results at 200 m/min presented by Puls et al. (2012), temperatures ranged only from 750°C to 1000°C during the time span in which friction coefficient was observed to be constant. Thus, it may be more accurate to conclude that the friction coefficient is insensitive to temperature over that specific high temperature range. Indeed, temperatures measured during the 20 m/min tests were considerably lower (250°C to 350°C), and the friction coefficient notably higher.

Strengths of this tribometer include the measurement of temperature close to the tool-workpiece interface and the generation of virgin, chemically active surfaces in the workpiece. However, the test duration is very short (less than 1s) and there is no mention of the normal and shear stresses involved, just the forces.

Similarities in the aforementioned experimental tribometers include the use of industrial scale cutting machines; an 'open' tribosystem approach whereby new material is constantly brought into contact with the tool material; and quantifying a friction coefficient as a function of relative sliding speed. In contrast, the tribometer developed by Biksa (2010) for the MMRI is a dedicated, bench-scale unit; it is also a 'closed' tribosystem, as the tool material contacts the same region of workpiece material

throughout the test duration; lastly, Biksa relates a coefficient of friction to temperature under elevated compressive stress at extremely low sliding velocities.

   The physical construction of the heavy load, high temperature tribometer developed by Biksa will be discussed in greater detail in Chapter 3. As a general overview, however, he loaded a polished, spherical tip pin made of tooling material into a flat, ground disc made of workpiece material, generating high levels of plastic deformation and normal contact stress. The stationary pin was axially aligned to within 0.01mm of the axis of the spindle used to rotate the disc relative to the pin. An induction heating coil positioned around the pin was used to raise the interface temperature, an estimation of which was obtained via infrared pyrometer measurement at a spot about 2mm above the interface on the pin. Measurement of the applied load F_N, reaction torque M_{TOT} required to shear the pin-disc interface, and the resulting diameter of the spherical imprint in the disc D_{IND} enabled calculation of mean normal stress, frictional shear stress, and coefficient of friction (COF) at the pin-disc interface according to the following equations (Biksa, 2010, pp. 114-116):

$$\sigma = \frac{4F_N}{\pi D^2{}_{IND}}$$
Equation 2.11

$$\tau_{AVG} = \frac{12M_{TOT}}{\pi D^3{}_{IND}}$$
Equation 2.12

$$COF = \frac{\tau_{AVG}}{\sigma} = \frac{3M_{TOT}}{F_N D_{IND}}$$
Equation 2.13

The equations presented above are in a slightly different form than those derived mathematically by Biksa, who used imprint radius R_{IND} instead of imprint diameter D_{IND}.

Biksa interacted both uncoated and TiAlN coated WC-6Co pins against flat, ground specimens of Ti6Al4V and Inconel 718 under a load of 1900N and from room temperature to about 700°C, rotating the disc on-axis relative to the pin at 1RPM for 10s. He established curves of coefficient of friction versus temperature for different tool-workpiece material pairs, which are reproduced in Figure 7.

Biksa attempted to link improved tool life using the TiAlN coating on cemented carbide tools to a reduced friction coefficient observed at some elevated temperatures. Unfortunately, temperature measurements were not made during the cutting experiments. As well, other indications of reduced tool-chip friction, such as reduced tool forces (Trent & Wright, 2000, pp. 77-79), were not noted. Instead, Biksa cited a 4th order relationship between the adhesive wear coefficient and the coefficient of friction as observed by Rabinowicz as a possible explanation. Upon closer inspection, this empirical relationship applies to sliding friction (Rabinowicz, 1995, Ch. 6), presumably lightly loaded sliders.
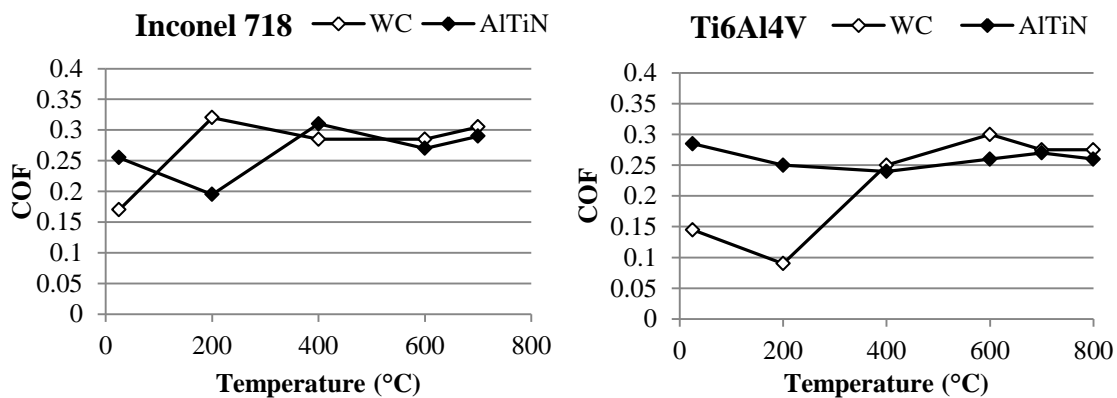
Figure 7: COF vs. Temperature Plots at a constant load of 1900N, adapted from Biksa (2010)

However, Biksa suggests that the tribometer interacts tool and workpiece materials under conditions relevant to those at the tool-chip interface where seizure is prominent, (2010, p. 174) which is characteristic of heavily loaded sliders as proposed earlier by Shaw. As such, this COF cannot be treated as a classical frictional coefficient; reporting of the mean normal stress and average shear stress is equally as critical. The same could be said for the results of the previous research groups.

The difficulty comes, however, if the interfacial bond between tool/coating and workpiece material becomes so strong that it is energetically more favourable for bonds to break and shear to occur internal to the workpiece material. Indeed, this is characteristic of seizure between the tool and chip in real machining. However, for a given temperature, the degree of strain and strain rate hardening within the chip adjacent to the tool is likely much higher than that experienced by the workpiece material adjacent to the pin in the tribometer. There is thus a danger in feeding these values into FE simulations of metal cutting. If the tribometer-predicted tool-workpiece material interfacial shear strength is really just the workpiece material flow stress under less severe strain and strain rate conditions, then FE simulations may predict sliding instead of sticking once sufficient strain and strain rate hardening occurs. As such, FE simulation results based upon temperature dependent COF or shear strength values from tribometer tests must be carefully validated.

It stands to reason that greater analysis of the tribometer results needs to be conducted in order to understand how they can be applied to prediction of tool life and FE modeling of metal cutting. Furthermore, links between COF as measured on the tribometer and tool

life data from machining tests can possibly be strengthened by tool force measurement, a

reduction in tool forces indicating improved tribological conditions at the tool-chip

interface for the same geometry of tool and cutting parameters.

Chapter 3. Modifications made to MMRI Tribometer Hardware and Software

3.1 Overview of the MMRI Tribometer Prior to Modifications

Biksa made a number of useful changes to the tribometer from its original state when initially purchased, which are described in detail in his Master's Thesis (Biksa, 2010). A brief summary of the tribometer functionality achieved by Biksa is presented below, and a visual overview of the various hardware components is presented in Figure 8.

The setup involves a flat disc made of the workpiece material gripped by a four-jaw chuck mounted on top of the spindle; and a pin made of tool material gripped in a collet assembly, which is permanently bolted in axial alignment to a Kistler 9329A reaction torque sensor.
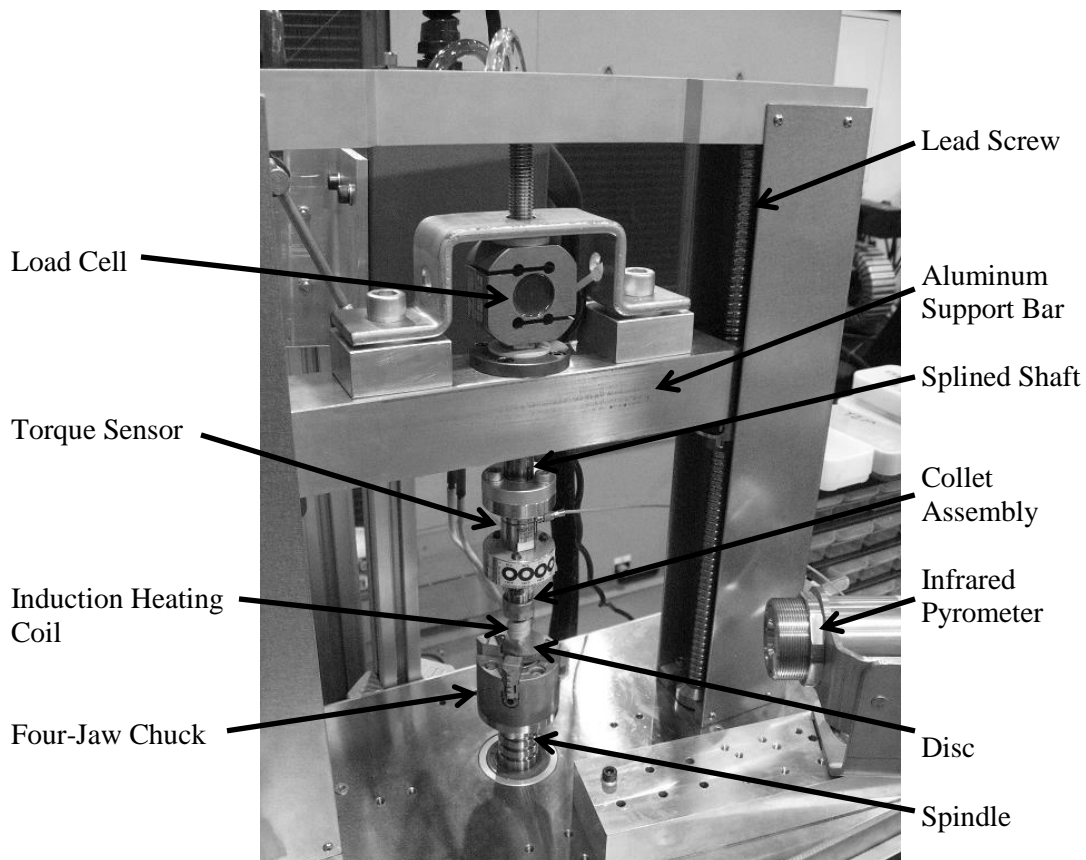
Figure 8: Overview of tribometer hardware implemented by Biksa

Three screws fasten the torque sensor to an upper mounting flange, which itself is press fit over a splined shaft. A 2500N rated strain-based load cell threads onto the other end of the splined shaft, which itself is free to translate up and down through the thick aluminum support bar. This bar is supported on either end by a lead screw. The screws are rotated by a DC motor via a timing belt, located beneath the stainless steel platform, which serves to syncronize the rotation of the screws to keep the arm level as it is raised or lowered. When the support bar and load column (the load cell, splined shaft, torque sensor, collet and pin) is lowered sufficiently such that the tip of the pin meets the flat disc, there is a range of motion over which the support bar moves indepent of the load column. Thus, the contact load is momentarily just the weight of the load column itself, until the support bar is lowered sufficiently that the bracket makes contact with the top of the load cell. At this point, further downward motion of the support bar transfers force through the load column, increasing the load experienced by the column and enabling the pin tip to make a spherical impression in the comparably softer disc.

The spindle, on which the four-jaw chuck is mounted, is actuated by a DC motor via a belt and pulley configuration located beneath the stainless steel platform. Engaging the spindle provides rotation of the disc relative to the stationary pin; the torque required to shear the pin-disc interface is sensed by the Kistler 9329A reaction torque sensor mounted within the load column. The torque sensor is rated to measure torque within the range of -1 to 1 Nm and, depending on the amplification setting of the accompanying charge amplifier, has a resolution down to 0.000005Nm (Biksa, 2010, p. 133).

Heating of the pin-disc interface is accomplished using an induction heating coil positioned around the pin. The coil itself is made of thin copper tubing, covered with an insulating sleeve. An associated power supply unit can send upward of 300A through the coil at a variable radio frequency, inducing eddy currents and heat generation within the pin. The temperature of the pin about 2 mm above the pin-disc interface is measured via an infrared pyrometer capable of temperature measurement up to 1000°C and the application of a special constant emissivity black paint near the pin tip.

A PIXSYS ATR423 Temperature Controller with closed-loop PID capabilities is used to regulate the current drawn through the induction coils in order to achieve a given temperature setpoint at the measured location near the interface. In practice, however, Biksa could only obtain controlled temperatures up to 800°C using pins made of cemented carbide loaded against discs under 1900N load (2010, p. 167).

The applied load and spindle speed are governed by separate closed-loop PID controllers built into the proprietary software provided by the original tribometer designers. This software interfaces with the National Instruments PCI 7354 Motion Controller hardware module installed in the PC.

3.2 Overview of Software Prior to Modifications

Biksa relied on proprietary software provided with the tribometer to control all kinematic and dynamic aspects of the tribometer. However, the thermal aspects of the original tribometer were replaced with the induction heating coil and infrared pyrometer mentioned above. The torque sensor installed in the load column was also a new feature.

Not being able to access the underlying programming scripts, he could not integrate all of the new components into the existing software. He thus created a simple data acquisition program using NI Labview to log measurements of load, torque and temperature acquired via a multi-channel analog voltage input module. His experimental method involved toggling switches and clicking buttons on various pieces of hardware and software. Integrating and automating control and data acquisition from all the key hardware components into a single piece of software was expressed as a desirable improvement to his setup.

3.3 Selection and Integration of Resistance Welder into Experimental Setup

One recommendation from Biksa (2010, p. 177) was to increase the heating capacity of the tribometer in an attempt to achieve elevated interface temperatures in the range of 800°C to 1000°C; he suggested either purchasing and integrating an electrical resistance spot welder into the setup, or replacing the existing 1kW inducting heating power supply with a more powerful 2kW unit. The pros and cons of both options were considered.

With induction heating, a coil of copper tubing is positioned around the metal object to be heated. Alternating electrical current flowing through the coil generates an electromagnetic field inside the coil, inducing eddy currents to flow within the metal object. In the case of the tribometer, the object positioned inside the coil is a pin, typically made of WC. In order to facilitate temperature measurement near the pin-disc interface via the infrared pyrometer, the coil must be positioned somewhat above this interface. Thus, heat is generated within the bulk of the pin and conducts down to the pin-disc

interface due to thermal gradients. This is analogous to heat being generated within the bulk of the tool and conducting to the tool-chip interface and is not representative of the thermal aspects of machining.

With electrical resistance heating, the cables of a resistance welder would be carefully attached to the tribometer to allow for electrical current to be drawn through the pin-disc interface while not impacting the instrument; the pin and disc actually form part of the electrical circuit. Heat is generated all throughout this electrical circuit (all cables plus pin and disc) according to:

$$\dot{Q} = I^2 R \qquad\qquad \text{Equation 3.1}$$

where $\dot{Q}$ is the rate of heat generation, I is the current drawn through the electrical circuit, and R is the resistance of the electrical circuit. The resistance of a conductor can be expressed as:

$$R = {\rho l}/{A} \qquad\qquad \text{Equation 3.2}$$

where ρ is the resistivity of the material, l is the length and A is the cross-sectional area of the resistor/conductor. In the pin and disc portion of the circuit, the cross-sectional area is smallest at the interface where the pin tip and disc contact; heat generation should thus be highest here and drop considerably toward the bulk of the pin and the disc. Similarly, temperatures should be highest at the interface and decrease toward the bulk of the pin and the disc. Thus, thermal gradients will be at least qualitatively similar to those present

in machining, wherein temperatures are highest at the tool-chip interface and decay further into the tool.

In regards to setup and integration of new equipment, upgrading to a 2kW induction heating power supply would be very straight forward. In contrast, integrating a resistance welder into the setup would require significant redesign of the load column and the spindle to allow for attachment of bulky electrical cables as well as to electrically isolate sensors, electronics, and the tribometer frame from the high levels of electrical current flowing in the system.

While the existing 1kW induction heating power supply is capable of supplying 300A of alternating current, it was frequently observed during experimentation with WC pins that the maximum current drawn would not exceed 180A. This is likely due to the relatively high electrical conductivity of WC; some experimentation with pins made of carbon steel (whose conductivity is somewhat lower) saw the full 300A of current drawn through the coil upon request. Thus, even though a 2kW unit would be more powerful, it was uncertain whether it would lead to the required increase of heat generation for similar reasons.

In the past, the MMRI has collaborated with Prof. L.S. Shuster from the Russia New University, who constructed and performed testing with a tribometer similar in nature to that developed by Biksa. As his method of heat generation was via a resistance welder, and as he commonly reports friction measurements at temperatures as high as 1000°C, there was little doubt that a resistance welder of adequate power capacity would be able to provide the increased heat generation required.

As a summary of the above discussion, Table 3 restates the main pros and cons of the two alternatives considered. In three of the four categories, moving forward with electrical resistance heating was deemed to be the most favourable approach.

Table 3: Summary of Pros and Cons of Induction Heating vs. Resistance Heating

Criterion	Upgrade to 2kW Induction Heater	Purchase Resistance Welder
Ease of Integration	**Simple:** the tribometer was already designed with induction heating in mind	**Complex:** welder must have remote receptacle to receive 0-10V command signal and open/close contact signal from PC; electrical cables must be attached to tribometer safely and sensors/components electrically isolated
Ability to Heat WC Pins to above 800°C?	**Possible but uncertain:** similar issues with the 1kW unit (set point of 300A but max output of only ~160A) may persist with 2kW unit	**Yes:** already validated by Shuster
Thermal Gradients Representative of Machining?	**No:** heat generated in bulk of pin (where coil located) and flows down to interface and disc	**Most likely:** heat generation will occur all throughout pin and disc, but is expected to be concentrated at pin-disc interface; temperatures should be highest at the pin-disc interface
Cost	**$3000 to $4000** (Biksa, 2010, p. 177)	**$1000 to $3000** (based on survey of welders at lincolnelectric.com and millerwelds.com)

Based on a description of Shuster's tribometer translated by Dr. G. Fox-Rabinovich, it was estimated that a welder capable of at least 300A be selected. In order to facilitate fully automated control via a PC, a method of activating and deactivating as well as regulating the current drawn from the welder was considered essential. A few local welding equipment suppliers were contacted in hopes of acquiring a rental unit with the aim of concept validation and more clearly determining necessary technical specifications. To this end, a refurbished Miller Gold Star 500SS DC welding power supply (Figure 9) was acquired on loan from Weld Tech Products Incorporated. Although it was an old unit (dating back to the late 1970's), it featured a 5-pin remote receptacle

which enables the user to regulate both the opening and closing of internal contacts as well as the amount of current drawn from the unit.
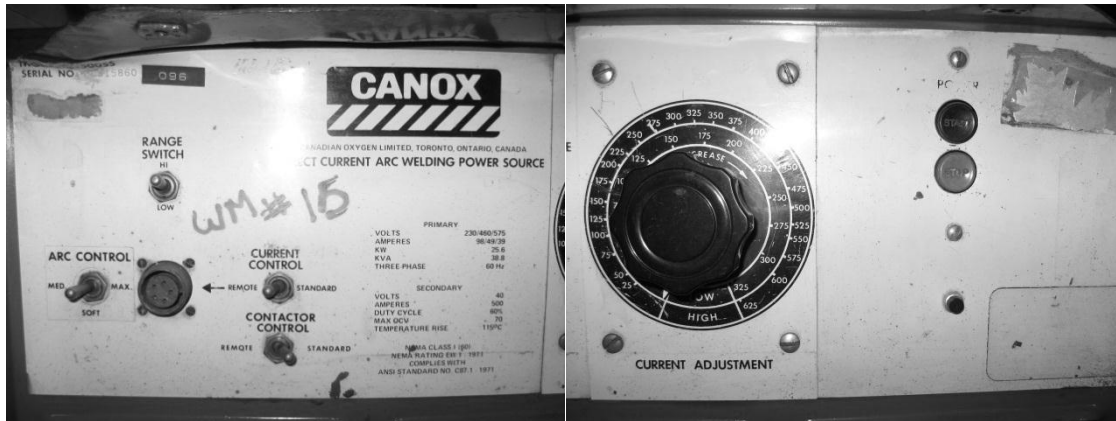
Figure 9: The Miller Gold Star 500SS DC welder used for concept validation

The supplier indicated uncertainty with regard to the actual current output at a given dial setting. As such, a 0.33mΩ shunt resistor and a voltmeter were connected across the positive and negative terminals of the welder; the actual current drawn could then be calculated according to Ohm's law, $I = V/R$. It was observed that considerably more current was drawn than that suggested by the current dial position. As such a map of set point (dial position) versus actual current drawn was established.

Next, the remote receptacle was wired to receive a 0 to 10V signal from an available DAC output channel on the NI 7354 Motion Control Board. To provide safety in interfacing between the PC and this high power welder, a Dataforth isolated voltage module was purchased. The current dial on the welder was turned to its maximum limit and tests were conducted using a 0 to 10V command signal from the PC to draw a fractional amount of this maximum current, recording the voltage across the shunt resistor in order to map the actual current drawn to the command signal.

Lastly, the welding cables were carefully attached to the tribometer in order to draw

current through the pin-disc interface so as to achieve electrical resistance heating. As a

first design concept (see Figure 10), a small plastic disc and an aluminum plate were

inserted between the torque sensor and the collet assembly, as well as between the spindle

flange and the four-jaw chuck. As well, a special four-screw aluminum jig was designed

in order to facilitate easy installation and alignment of the collet assembly. Nylon screws

were used for fastening and the order of the plastic disc and aluminum plate was such as

to electrically isolate the rest of the tribometer, ensuring current would flow only through

the collet assembly, pin, disc and four-jaw chuck. The bulky welding cables were

carefully bolted onto the aluminum plates.
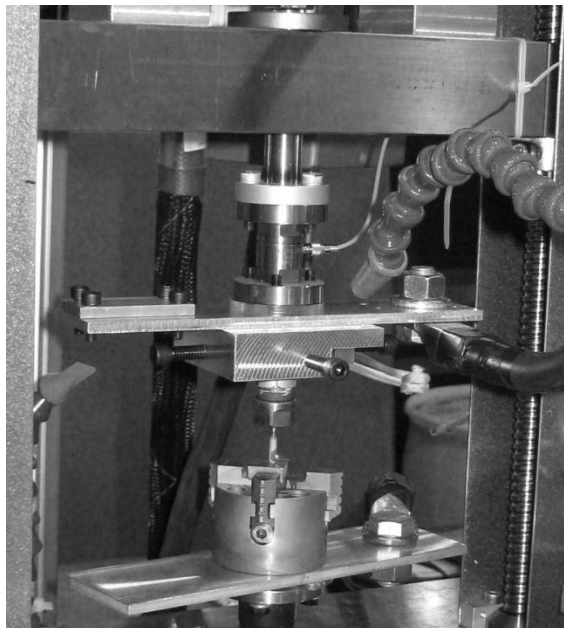
Figure 10: First design concept for attachment of welding cables to tribometer

A WC-Co pin was loaded up to 1500N against a small disc made of H13 tool steel.

Testing commenced at a 1V command signal (~60A) for 60s or until the measured

temperature achieved steady state. At 3V (~140A), the temperature stabilized around 600°C. At 4V (~175A), the temperature surpassed 900°C and continued to climb, so the test was halted prematurely so as not to surpass the sensor limit.

Based on this testing, it was determined to source a DC welding unit that had similar features to this demo unit (remote receptacle allowing automated opening and closing of internal contacts, as well as regulation of output current); however, the new unit should be considerably smaller, both for space constraints as well as to ensure sufficient resolution of output current using a 0 to 10V command signal. Examining the test results, a 200A unit was deemed too have sufficient current capacity to achieve 1000°C at the pin-disc interface. After a lengthy search, a Miller Maxstar 200 SD was sourced and purchased through Weld Tech Suppliers Inc.

There were some concerns, however, with the initial design concept for the attachment of the welding cables to the tribometer; namely, the risk of overloading the torque sensor (whose damage threshold is only 1.2Nm) when fastening or unfastening the welding cable from the upper aluminum plate; the influence of the cable weight and residual twist on the torque sensor reading during tests; and the restriction of rotational distance imposed by the cable fastened to the lower aluminum plate.

It was thought beneficial to try to fasten the bulky welding cable to a separate mounting location and run thinner "jumper" cables between this mounting location and the aluminum plate. Jumper cables were made by cutting a small length of the bulky welding cable, removing the insulation and twisting the fine copper strands into sixteen slightly larger-diameter conductors. In this way, the same cross-sectional area of copper

wire was being used as in the welding cable itself, which was rated for well over 200A of current.

As there were some pre-existing holes threaded into the back of the aluminum support bar, this was chosen as the mounting location. A special mounting pad was fabricated that provided electrical isolation between the cables and the aluminum support bar, and that facilitated easy fastening and unfastening of the welding cable without disturbing the jumper cables. The physical implementation of this design is shown in Figure 11.

Figure 11: Second design concept for attaching upper welding cable to tribometer

It was decided to design a new mounting location at the top of the load column, above the torque sensor, as shown in Figure 12. One end of a rectangular steel plate was sandwiched between two thin plastic discs and inserted into the load column between the torque sensor and the mounting flange of the splined shaft. This assembly was fastened together with nylon screws to ensure electrical insulation. Jumper cables were clamped between this steel plate and the existing aluminum plate. Similar to the previous
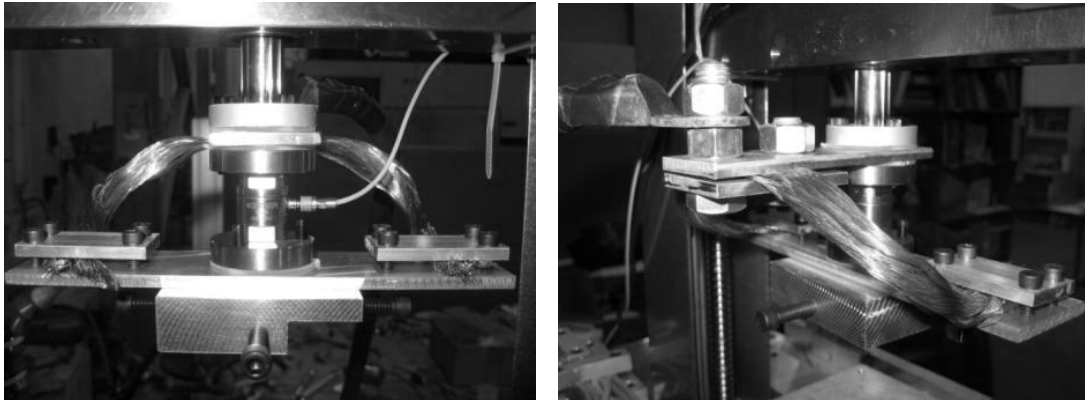
Figure 12: Third design concept attaching upper welding cable to tribometer

configuration, the bulky welding cable can be easily fastened and unfastened without

disturbing the jumper cables and upsetting the equilibrium of the torque sensor. This

configuration ensures that the fastening and unfastening of the welding cable does not

transmit any torque through the sensor. Furthermore, the jumper cables do not stretch and

contract during loading/unloading of the pin. As such, variable cross-talk during testing is

avoided. However, the clamping pressure at the interface between the flanges, plastic

discs, and steel plate is not as high using nylon screws as it would be with steel screws. It

is important for the operator to use two wrenches and apply the equal-but-opposite torque

principle when fastening or unfastening the welding cable, lest the torque sensor be

shifted out of axial alignment with the spindle.

While there were no concerns about excessive torque when fastening the second cable

to the bottom aluminum plate, this connection did limit the rotational freedom of the

spindle, constricting it to about only 1/4 of a full rotation. To allow for maximum

flexibility in testing, a modified means of conducting current from the specimen to the

ground cable needed to be developed to allow for at least one full spindle rotation.

One possible concept included a conductive bushing or bearing to be positioned around the four-jaw chuck. This would be similar in nature to the use of graphite brushes in brushed DC motors. However, there was concern about achieving sufficient contact pressure and sufficient conductor cross-section area to allow 200A of current to pass. It was decided instead to connect several long, small-diameter conductors between the rotating assembly and a stationary mounting pad. As the spindle rotates, the conductors coil themselves around the assembly. It was found that 8 conductors, with their insulating sleeves still intact, could be wrapped around the spindle approximately 3 times before becoming inoperable. While the total cross sectional area of these 8 conductors is about half that of the welding cable, it was reasoned that the relatively short duration of tests (< 60 seconds) at even maximum current (200A) would not result in overheating of the cables, which has proved true in practice.

A new platform for holding specimens was designed and installed on the spindle. Altogether, it is about 10 mm shorter in height than the previous configuration with the four-jaw chuck, which frees up considerable vertical space. The new platform is approximately 30-mm thick, giving an additional 10-mm of vertical space. The cables fasten to the platform and the stationary mounting pad. The new configuration can be seen in Figure 13.
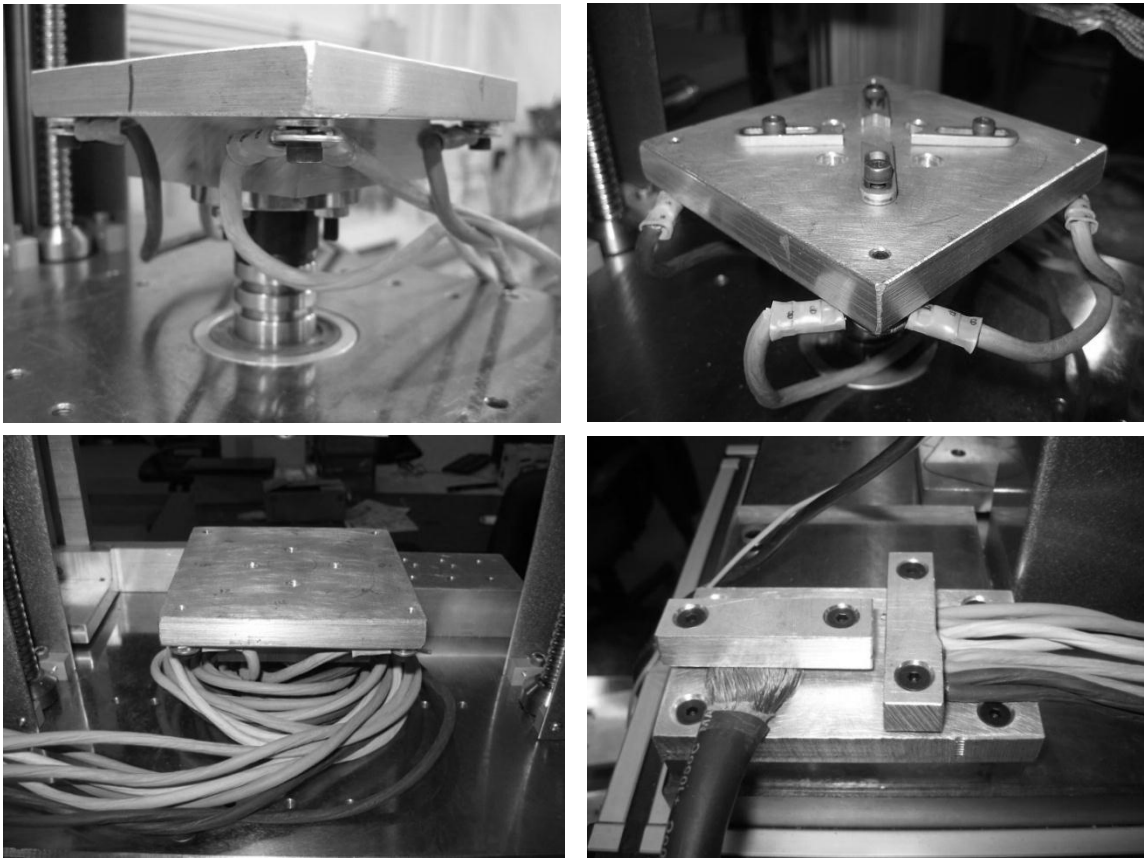
Figure 13: Second design concept for attaching lower welding cable to tribometer.

3.4 Development of a New Graphical User Interface

Extensive work was performed to identify the function of various electronic

components within the hardware boxes accompanying the tribometer and to map analog

signal flow between each of these components and the NI 7354 Motion Controller. With

this accomplished, a new Graphical User Interface was developed on NI Labview to

provide synchronous control, measurement, display and logging of key variables such as

load, spindle speed, and temperature. A screenshot of the front panel of the GUI is shown

in Figure 14 and a screenshot of the block diagram view of the GUI can be found in the

Appendix. Efforts were made to ensure that all of the useful features of the previous

control and data logging software used by Biksa were preserved, while at the same time

adding new and beneficial features. A fully automated test mode (described in more detail

later) as well as a fully manual, user-prompted test mode provides the user with flexibility

in how to run tests, all with the ease of clicking buttons on the GUI instead of flipping

switches on different pieces of hardware. As well, more sophisticated logic was

incorporated into the underlying structure to provide safety and protection for the user

and the hardware. A comparison of the existing performance of the software used by

Biksa and the improved capability with this new GUI is presented in Table 4.
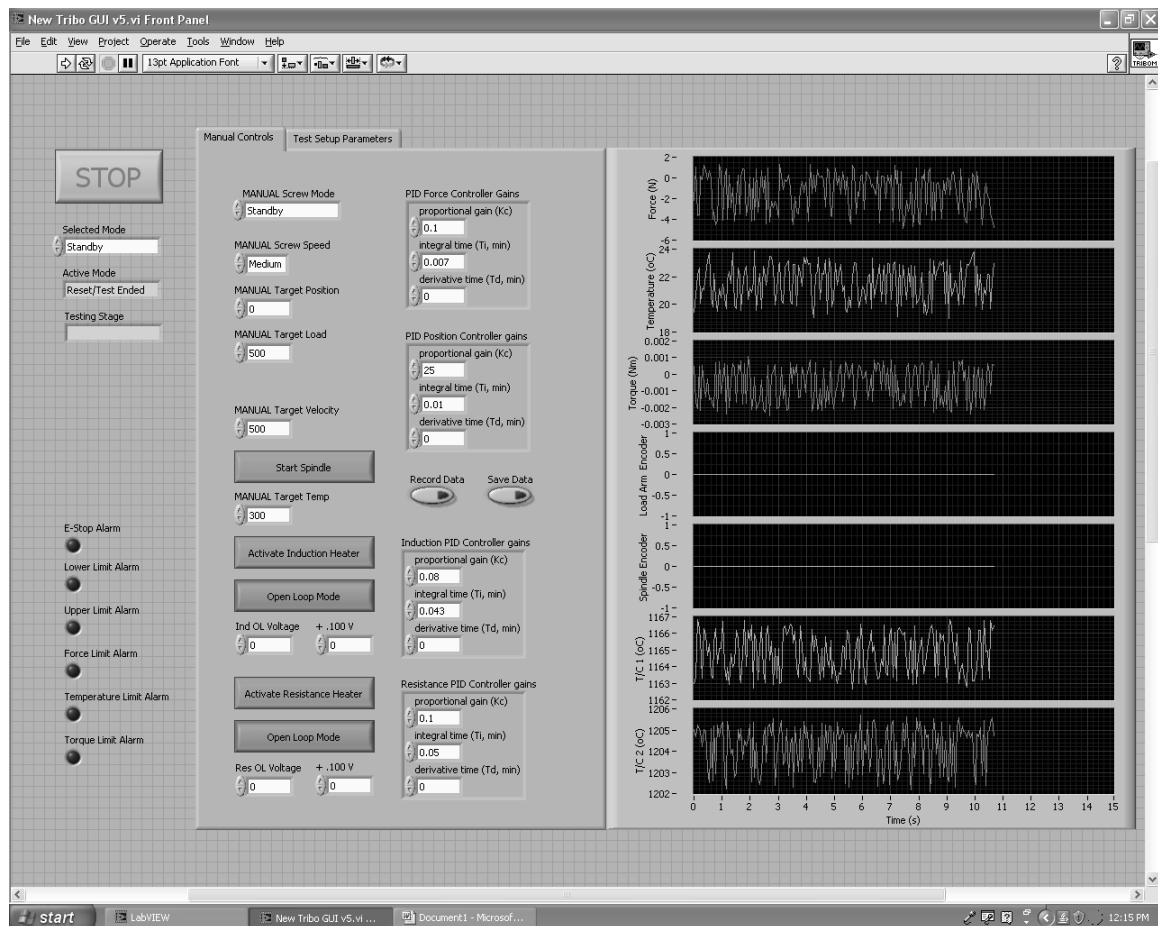
Figure 14: Front panel view of Tribometer GUI

Table 4: Comparison of tribometer features before and after GUI development

Feature	Existing Performance	Improved Capability
Automated test sequence	Data logging software separate from control software; Preload must be manually applied; Heating activation performed manually and controlled via separate hardware; Only PID load control available.	Data logging and control integrated into one GUI; Preload and heating activation integrated into automated test sequence; Heating control integrated into GUI; PID control of load or position available.
Manual Mode	Can manually raise or lower load arm or specify a target position; No direct load control capability; Unable to activate spindle.	Can manually raise or lower load arm; PID control of either load or position available as well; Spindle can be activated.
Spindle Jerk	Spindle would rapid to 'home' position at the start of automated test sequence.	Spindle 'home' position is reset whenever activated, eliminating undesirable jerk.
Load Cell Safety And Maximum Allowable Load	Automated test sequence would safely abort if load increased above fixed threshold of 2000N; In manual mode, user could accidentally overload the load cell (>2500N).	In both manual mode & automated test sequence, GUI switches to safety mode, deactivating load column motor, if load exceeds user-specified threshold (currently programmed at 2400N)
Torque Sensor Safety	During installation/removal of pin from collet, user must monitor torque signal to ensure it does not exceed 1 Nm (damage threshold is 1.2 Nm); User must manually abort test sequence if torque rising too high.	During installation/removal of pin-collet in 4-screw jig, user must monitor torque signal to ensure it does not exceed 1 Nm (damage threshold is 1.2 Nm); In both manual mode & automated test sequence, spindle motor automatically deactivated and tribometer switches to safe mode if measured torque exceeds 0.95 Nm.

An overview of the automated test sequence is summarized below.

Step 1 – Preload

Data recording is initiated. Values of load, temperature, torque, lead screw motor encoder position, and spindle motor encoder are stored in an array, which will later be written and saved to a data file in *Step 7*. The pin is automatically brought into contact with the disc and loaded to the specified preload set point (i.e. 1000N). *Step 1* continues until the specified amount of time (i.e. 60s) has elapsed without the measured load leaving a specified tolerance band (i.e. +/- 10N) around the specified preload set point.

Step 2 – Heating

The specified heating equipment (i.e. DC welder) is automatically activated and the measured temperature on the pin begins to rise until it reaches and settles at the specified temperature set point (i.e. 500°C). Meanwhile, the force controller attempts to maintain the specified preload, although the load may likely momentarily spike upward at the onset of heating and fluctuate as the temperature settles toward its set point. *Step 2* continues until the specified amount of time (i.e. 5s) has elapsed without the measured temperature leaving a specified tolerance band (i.e. +/- 10°C) about the specified temperature set point.

Step 3 – Apply Full Load

The applied load may now be increased, maintained at the previously specified preload, or even reduced if so desired. Regardless, *Step 3* continues until the specified amount of time (i.e. 10s) has elapsed with neither the measured temperature nor the measured load leaving a specified tolerance about their respective set points.

Step 4 – Rotate Spindle

The spindle is now rotated at its specified speed (i.e. 1 RPM). Load and temperature controls are still operating to maintain their respective set points. *Step 4* continues until a specified time (i.e. 5s) or specified degree of angular rotation (i.e. 5000 spindle motor encoder divisions) has elapsed.

Steps 5 & 6 – Cooling, Shearing, Pin Retraction & Relay Deactivation

The spindle is then stopped and the heating unit deactivated. The specified full load is maintained for an additional 30s, which is hardwired into the logic. This allows time for the pin and disc to cool. After 30 seconds elapses, the spindle is engaged and rotates at 1RPM for an additional 2s. This is to shear any local welds that may have formed during the cooling phase. The spindle is then deactivated again and the pin is automatically retracted about 20mm, after which the lead screw motor is also deactivated.

Step 5 was originally a much simpler procedure and involved deactivating the spindle and heating unit and retraction of the pin without subsequent rotation of the spindle. However, it was found that the intensity of adhesion between the pin and disc during elevated temperature tests was often sufficient that the tip of the pin would break off under tensile stresses as the pin was retracted. It was thought desirable to try and first shear any welds by rotating the spindle under cooler conditions as opposed to breaking the interfacial bonds under pure tension when the pin was retracted.

Step 7 – Save Data

The user is prompted to specify a folder and file name for the data measured since the start of *Step 1* through to the completion of *Step 6*.

Chapter 4. Development of Experimental Procedures

Biksa used a load of 1900N and rotated the spindle at 1RPM for 10s in his tests (2010, p. 153). While explaining the rationale for selecting these parameters, he appears not to have conducted a systematic study on the influence of different parameters on the results yielded by the tribometer. As such, it was deemed appropriate to explore the sensitivity of output variables (imprint diameter, reaction torque, normal stress, shear stress, and COF) on the input variables selected (applied load and duration, applied temperature and duration, spindle speed and duration, pin and disc materials) in order to gain greater confidence of the accuracy and significance of the tribometer results.

4.1 Hard Pin on Soft Disc Configuration

4.1.1 Influence of Normal Load on Achievable Contact Stress

The normal load applied during testing is one of the most significant input parameters. A set of 'static' tests (without any rotation) were performed at room temperature using a standard 3mm spherical tip WC pin loaded against flat, polished discs of AISI 1045 steel. Applied loads ranged from 125N to 2000N and were maintained for 60s, after which the pin was retracted. The diameter of the resulting imprint was measured using an optical microscope. Similar testing was performed using flat discs made of Inconel 718, Ti6AlV4 and AA6061 in order to investigate this trend with materials of greater and lesser hardness. Figure 15 illustrates the range of normal stresses achieved in relation to the applied load, where normal stress was calculated according to Equation 2.11.
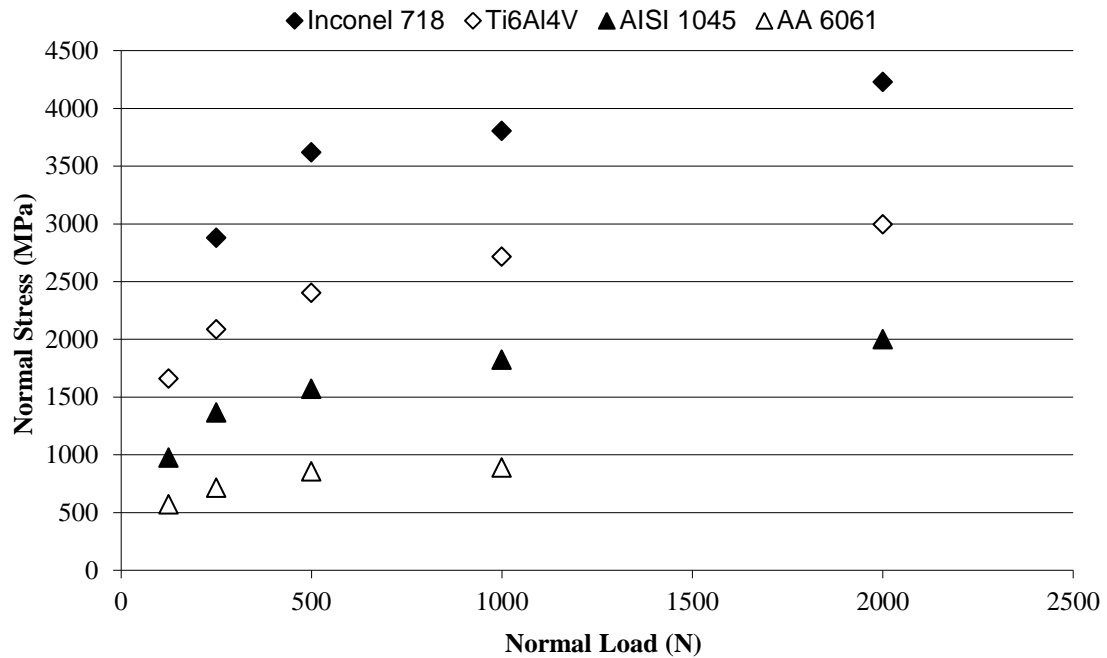
Figure 15: Influence of applied load on achievable normal stress

Inconel 718 is a nickel-based superalloy and Ti6Al4V is an aerospace grade of

titanium alloy. Both materials maintain their high strength properties up to fairly elevated

service temperatures. AISI 1045 is a medium-carbon grade of steel, whereas AA 6061 is a

structural grade of aluminum alloy. The trend for each of these materials in Figure 15 is

qualitatively similar. The mean normal contact stress increases as the applied normal load

increases; below a 500N load, the mean normal contact stress is quite sensitive to the

applied normal load; above a 500N load, the increase in mean normal contact stress with

applied normal load is much less severe. As can be seen in Figure 5, the range of

achievable mean normal contact stress on the tribometer is roughly 2 to 4 times the yield

strength of the material.

Table 5: Table of material yield strength and achievable stress range on tribometer

Material	Yield strength	Achievable stress on tribometer
Inconel 718	[a]1110 MPa	2900 – 4250 MPa
Ti6Al4V	[b]830 – 1070 MPa	1650 – 3000 MPa
AISI 1045	[c]300 – 450 MPa	975 – 2000 MPa
AA 6061	[d]180 – 340 MPa	570 – 900 MPa

[a] (Ezugwu, Bonney, Fadare & Sales, 2005)
[b] (as seen in Rack & Qazi, 2006)
[c] (Tata Steel International)
[d] (Dorward & Bouvier, 1998)

Applying a lighter load, while generating a lower mean normal contact stress, also generates a smaller imprint diameter, which can be disadvantageous from a measurement perspective, especially for harder materials. For example, under a 125 N load the imprint diameter in AA 6061 was 0.528 +/- 0.010 mm whereas for Ti6Al4V it was 0.310 +/- 0.010 mm. The absolute uncertainty, taken as the standard deviation of 4 measurements for 2 test replicates, or 8 measurements in total, is the same for both materials; however, the relative uncertainty (absolute uncertainty divided by the average measurement) is higher for Ti6Al4V (0.031) than for AA6061 (0.018). As the load is increased, the imprint diameter itself increases while the absolute uncertainty tends to decrease, so the relative uncertainty associated with the imprint diameter measurement decreases substantially. Thus, with the exception of extremely soft materials (AA6061), it is advisable to use loads in the range of 500 to 2000 N to avoid excessively small imprints. However, one drawback to using higher loads is the accompanying increase in friction and stiction in the lead screws of the tribometer, which manifests in poorer load control (see Figure 16).
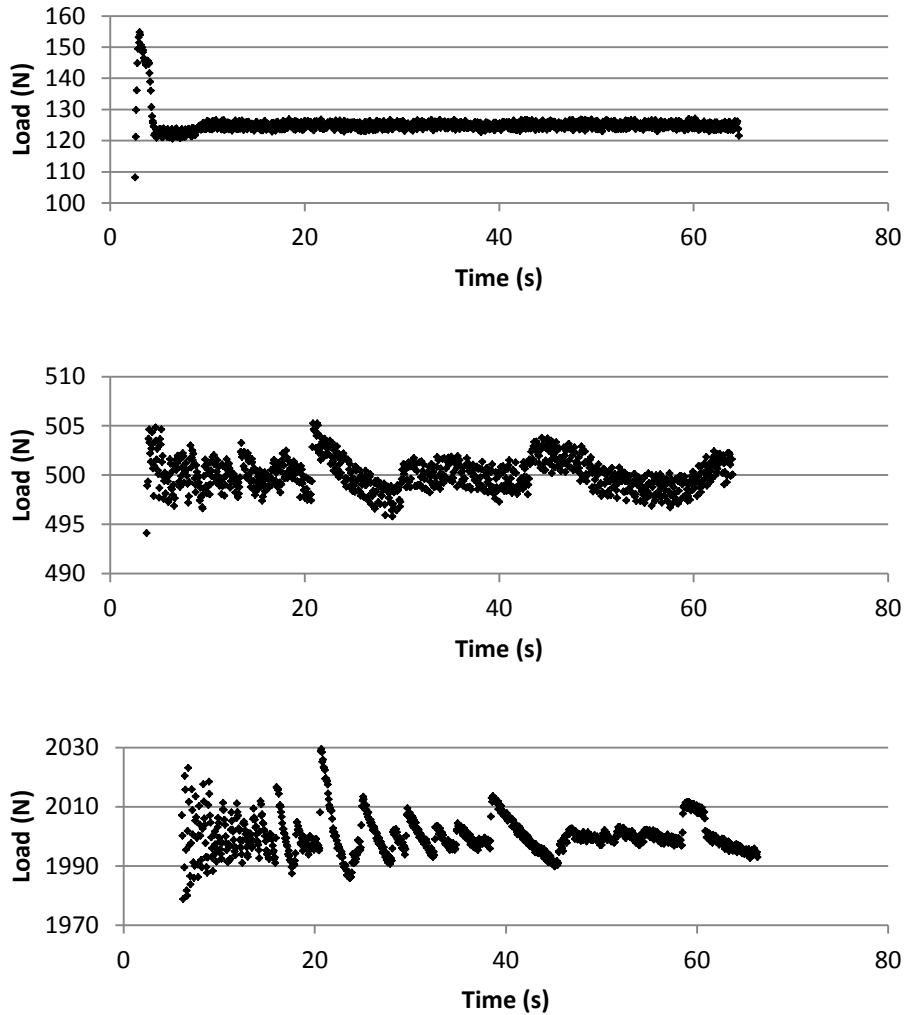
Figure 16: Variation in measured load at different load set points

4.1.2 Influence of Normal Load and Rotation Time on COF

Having established an appropriate range of loads (500N to 2000N), testing was

conducted to determine an appropriate length of time to rotate the spindle. For simplicity,

spindle speed was fixed at 1RPM to correspond with tests performed by Biksa (2010, p.

153), and testing was performed at room temperature. After an initial 60s of static load,

the spindle was rotated for 60s (corresponding to 1 complete spindle revolution) while the

target load was maintained. After an initial jump at the onset of rotation, the torque signal

increased in an approximately linear manner throughout the rest of rotation. Another set

of tests was conducted, this time limiting rotation to only 1s. Table 6 highlights the

variation in some of the output variables with respect to normal load and rotation time.

Torque values reflect the average torque signal during the final 0.5s of rotation. For each

load tested, the increase in imprint diameter after 1s of rotation was negligible (~0.01mm)

and within experimental uncertainty of the imprint measured from the static tests.

Table 6: Influence of rotation time and normal load, WC pin vs. AISI 1045 disc

Load (N)	500			1000			2000		
Duration (s)	0	1	60	0	1	60	0	1	60
Dia. (mm)	0.63	0.64	0.76	0.84	0.85	1.00	1.12	1.14	1.33
σ (MPa)	1604	1554	1102	1804	1762	1273	2030	1959	1440
Torque (Nm)	----	0.013	0.045	----	0.032	0.111	----	0.086	0.340
τ (MPa)	----	189	392	----	199	424	----	222	552
COF	----	0.122	0.355	----	0.113	0.333	----	0.113	0.383

Similar testing was performed using an uncoated WC pin in contact with flat, polished

discs of Inconel 718. It was found that static testing under 2000N load maintained for a

range of 30s to 120s resulted in imprints with effectively the same diameter. Thus, normal

loads of 500N and 2000N were maintained for only 30 seconds, followed by rotation of

the disc at 1RPM for 5s and 20s. This time, three test replicates were performed for each

combination of load and rotation time, for a total of 12 tests. The torque responses for

tests at 500N and 2000N are shown, respectively, in Figure 17 and Figure 18. One can

observe the continued increase in torque values over the full 20s of rotation in the 500N

load tests. In contrast, torque values essentially plateau after 5s in the 2000N load tests.
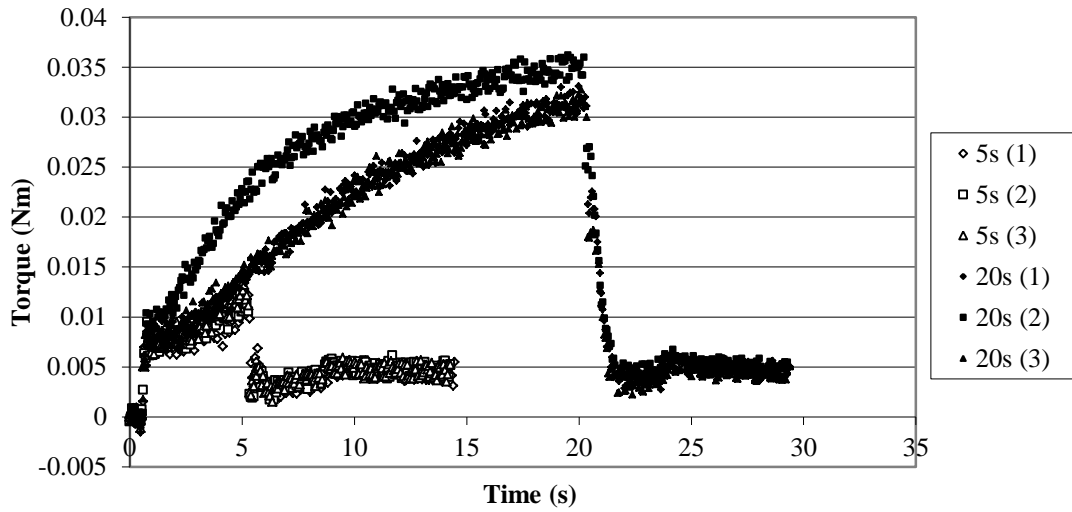
Figure 17: Torque responses for 500N load tests
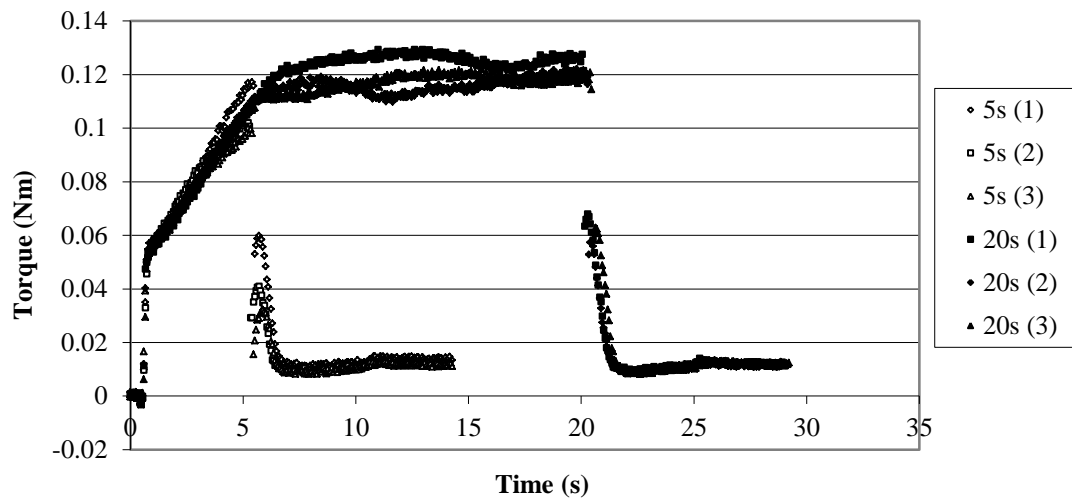
Figure 18: Torque responses for 2000N load tests

Table 7 presents the averages of the output variables with respect to normal load and

rotation time. Torque values in the "1s" columns are averaged over 6 tests (for the same

normal load) during the time interval 0.5 to 1.0s, while the imprint diameter is actually

that from the associated static test, based on results shown previously in Table 6.

Table 7: Influence of rotation time and normal load, WC pin vs. Inconel 718 disc

Load (N)	500			2000		
Duration (s)	"1"	5	20	"1"	5	20
Dia. (mm)	0.425	0.435	0.486	0.764	0.802	0.814
σ (MPa)	3525	3367	2699	4363	3962	3846
Torque (Nm)	0.008	0.011	0.028	0.060	0.105	0.122
τ (MPa)	402	521	916	517	777	862
COF	0.114	0.155	0.339	0.118	0.196	0.224

Looking at Table 6 and Table 7 together, the trends are qualitatively similar. The COF is independent of normal load when very short time duration (1s) tests are performed. Conversely, for longer test durations, COF values can vary widely and depend both on time duration as well as normal load.

The rise in COF with rotation time is due to an apparent increase in average shear stress and a decrease in average normal stress. Also noteworthy is the increase in imprint diameter with increasing rotation time. It was the suggestion of Wu (2011) that the increase in imprint diameter is the result of the tangential shear stresses initiated at the onset of rotation, causing the total stress state at the pin-disc interface to exceed that required for further plastic flow until a new equilibrium is established.

The decrease in normal contact stress is a direct result of the increasing imprint diameter and the constant normal load (Equation 2.12). One might expect that the average shear stress should also decrease, assuming COF to be constant as in classical sliding friction. Instead, the average shear stress increases as the imprint diameter increases, leading to a considerable growth in COF.

The cause for this increase in shear stress could be related to a growth in the *real* contact area as relative motion between pin and disc begins, combined with the penetration of residual surface contaminants leading to increased metal-to-metal

adhesion. This in turn could trigger the start of material transfer and adhesive wear particles ploughing through the workpiece material. Alternatively, slight misalignment of the pin axis relative to the spindle axis and/or geometric imperfections at the pin tip (flat spots, elliptical rather than spherical profile) could lead to workpiece material ploughing, thereby increasing the torque signal and the apparent average shear stress over time.

Some investigations into the cause for the increase in torque, imprint diameter and COF over the course of rotation were carried out nearer to the end of this research. An uncoated WC pin was loaded against a disc of AISI 1045 steel under 2000N for 60s followed by rotation for 60s at 1RPM. This test was repeated a few different times, both in a dry state and in a lubricated state by applying a few drops of mineral oil onto the disc prior to loading the pin against it. It was thought that the addition of oil would lubricate the interface; thus, if wear and material transfer were the driving cause for increases in torque and COF, the torque signature would be considerably more stable throughout rotation. If misalignment and ploughing of the pin was the dominant cause, it was thought that the added lubricant would not greatly influence the torque signature.

Figure 19 shows examples of the torque responses to both dry and intentionally lubricated cases. There was no discernible difference in the preparation of pin and disc for Test 1 – Dry and Test 2 – Dry; however, the torque signatures are dramatically different. The torque signal in Test 2 – Dry was consistently low, not showing any substantial rise over the full 360 degrees of rotation. The relatively constant torque signal for the first half of Test 1 – Lubricated and for the entire duration of Test 2 – Dry suggest that pin alignment errors cannot be responsible for the rise in torque signal commonly witnessed.

◇ Test 1 - Dry ▲ Test 1 - Oil × Test 2 - Dry
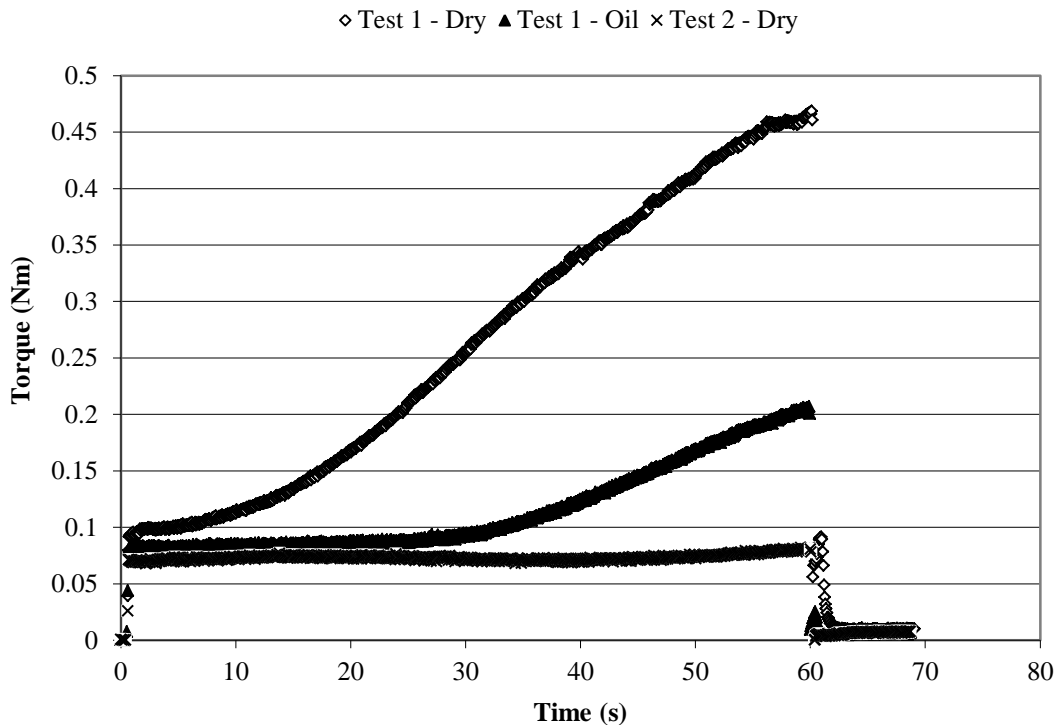
Figure 19: Dry vs. Lubricated Torque Responses

A more reasonable explanation is that of material transfer and the accumulation of wear particles tending to plough through material at the interface. This is supported by qualitative evidence from the resulting imprints themselves, as seen in Figure 20. The left hand image is that resulting from Test 1 – Dry, which shows considerably more smearing of the workpiece material at the interface. The imprint resulting from Test 2 – Dry is shown to the right and has a very smooth, shiny surface with next to no smearing. It is also considerably smaller in diameter.

Referring once more to Figure 19, it is striking that the tendency for the torque signature to increase correlates with the magnitude of torque at the start of rotation. Increased torque at the start is probably reflective of a higher degree of cleanliness, which
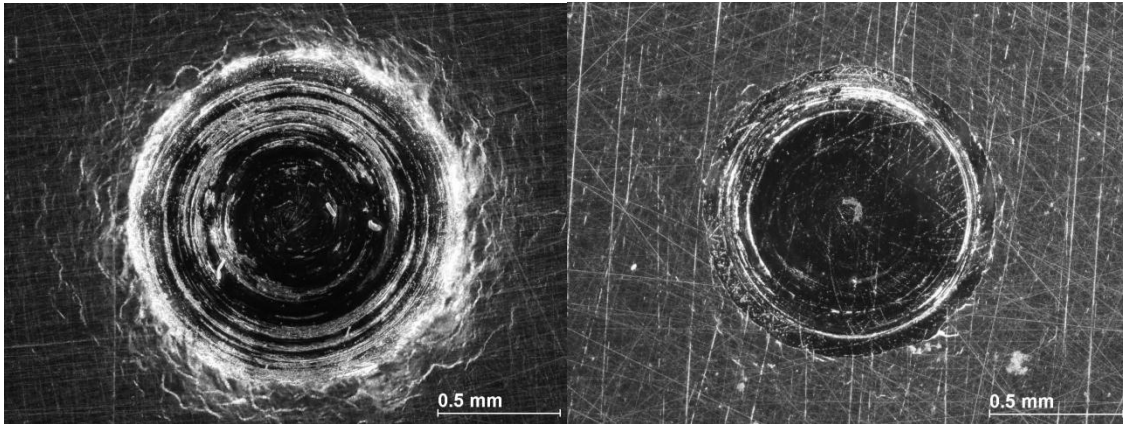
Figure 20: Resulting imprints of high friction (left) and low friction (right) tests

would better enable true metal-to-metal contact to be established and strong adhesion to occur. Thus, while care should still be taken to ensure that the pin is well aligned to the spindle axis, its influence on the torque signal is within acceptable experimental error. The increase in torque signature and the accompanying increase in COF is a result of friction itself. More effort will need to be invested in ensuring surfaces are consistently cleaned in order to achieve more repeatable results.

In light of the aforementioned discussion, there is evidence to suggest that it is beneficial to keep tests very short for the sake of repeatability, no more than 5s at 1RPM. For such short rotation time, the resulting COF is then insensitive to the normal applied load, and any increase in torque signature owing to adhesive wear itself will be minimized.

4.1.3 Influence of surface roughness of coated pins

Testing was performed using TiAlN-coated WC pins and flat, polished AISI 1045 discs under 500N load, room temperature conditions, and 5s of rotation at 1RPM. Two pins were subjected to five successive tests under these conditions. The first pin was

tested without preliminary polishing. The second pin was polished using aluminum oxide

paste under 5N load and 500RPM for 5 minutes prior to its first test, with no further

polishing between subsequent tests. Table 8 presents the results of these tests. The

calculated COF for the unpolished pins is 2-3 times that for the polished pins and tends to

decrease with successive tests. In contrast, the COF calculated for the polished pins

shows no such decreasing trend and has a notably smaller standard deviation over the five

measurements (polished – 0.012 vs. unpolished – 0.029). The reason for this discrepancy

is the improvement in surface finish provided by the preliminary polishing step. Figure 21

shows digital photographs taken via an optical microscope of the resulting imprints. The

imprint resulting from the unpolished pin is rough as a result of hard microdroplets on the

coating surface, characteristic of the deposition process. These microdroplets would tend

to increase the torque response as they plough through the soft workpiece material. The

imprint resulting from the polished pin is in contrast much smoother, with only a few

circular polishing grooves.

Table 8: Results of unpolished vs. polished, coated pin tips

Test Number	Torque (Nm)	Normal Load (N)	Diameter (mm)	COF
Unpolished, 1	0.0329	504	0.701	*0.279*
2	0.0310	503	0.667	*0.278*
3	0.0282	502	0.671	*0.251*
4	0.0277	500	0.674	*0.246*
5	0.0233	500	0.674	*0.207*
Polished, 1	0.0112	500	0.636	*0.106*
2	0.0082	498	0.606	*0.082*
3	0.0094	499	0.628	*0.090*
4	0.0114	499	0.617	*0.111*
5	0.0096	499	0.619	*0.093*
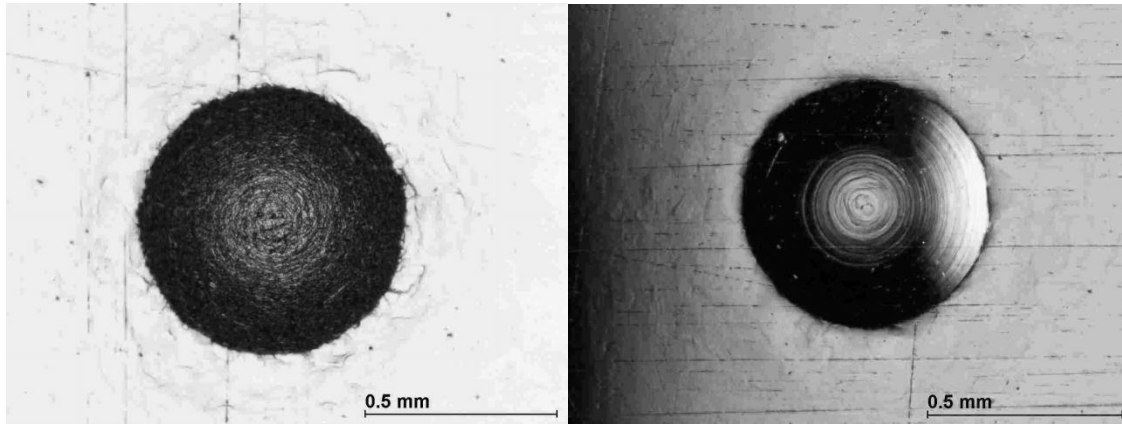
Figure 21: Disc imprint resulting from pre-polished (left) and post-polished (right) coated pin

It is thus imperative that coated pins first be polished prior to tribometer testing. This

is noteworthy – while Biksa recommended polishing in between subsequent tests with a

given pin (2010, p. 154), it is unclear whether coated pins were polished prior to their first

time use. Despite uncoated pins arriving from the manufacturer with a highly polished tip,

it might also be advisable to pre-polish these uncoated pins using the MMRI setup prior

to testing so that the surface roughness is comparable between subsequent tests.

4.1.4 Influence of Normal Load on Peak Temperature and Thermal Gradient in Pin

A WC pin was loaded against a flat disc of AISI 1045 steel under loads of 1000N and

2000N. After 2 minutes of constant current heating, infrared pyrometer temperature

readings were taken at three locations along the exposed length of the pin: near the pin-

disc interface; near the midpoint of the exposed length of pin; and near the pin-collet

interface. The results are shown in Table 9.

Table 9: Temperature variation along the length of the pin under constant current heating

Load (N)	Current (A)	Temperature (°C) Measured Near		
		Pin-Disc Interface	Pin Midpoint	Pin-Collet Interface
2000	60	53	58	56
	100	105	125	115
	160	320	380	320
	200	700	800	650
1000	60	70	77	70
	100	155	170	145
	160	495	535	420
	200	920	950	700
	200*	420	440	380
500	160*	205	180	135
	180*	425	400	300

* A stream of chilled air was directed at the gold collet nut in an attempt to provide greater cooling at the pin-collet interface.

Of primary concern was the observation of the maximum temperature occurring near the midpoint of the pin, not near the pin-disc interface. In an attempt to correct the thermal gradient and offset the heat generation within the bulk of the pin itself as well as at the pin-collet interface, a stream of chilled air was directed at the collet-nut and the test repeated with 200A of current and 1000N of load. This did not change the ranking of temperatures, but did substantially reduce the measured temperatures at each location by roughly 50%. It was later noted that further tightening of the collet led to consistently lower temperatures near the pin-collet interface as well as at the pin midpoint.

Secondly, the measured temperatures at each location were notably higher under 1000N of load as opposed to 2000N of load. This can mainly be attributed to the smaller imprint formed under 1000N of load, which corresponds to higher contact resistance and greater heat generation. With this in mind, further tests were conducted under 500N load, where it was seen that peak temperatures occurred near the pin-disc interface, as is desired.

Out of curiosity, testing was performed to try and quantify the potential drop at the

pin-disc interface, which is directly proportional to contact resistance. A constant current

of 60A was drawn through the setup and leads from a voltmeter were held against the pin

and the disc, respectively. Table 10 presents the voltage drop across the pin-disc interface

for various disc materials under varying normal loads. It clearly highlights the decrease in

contact resistance as the applied load is increased.

Table 10: Voltage drop across pin-disc interface for various disc materials and loads

Load (N)	Voltage drop across pin-disc interface (V)		
	AISI 1045	Inconel 718	TiAl6V4
250	.140	.205	.252
500	.120	.206	.215
1000	.060	.165	.181
2000	.032	.132	.155

As mentioned earlier, using 500N of load with AISI 1045 led to a favourable

temperature distribution in the pin, with maximum temperature observed closer to the

pin-disc interface. This corresponded to a potential drop of 120mV. Interestingly, the

potential drop observed for both Inconel 718 and TiAl6V4 discs under 2000N was

actually somewhat higher. When tested under various constant current heating, the

temperature profile in the pin was also favourable. Thus, a favourable thermal gradient

can be achieved in the pin using resistance heating provided that the applied load is

properly selected for the disc material. Under 60A current heating, the load should be

chosen such that the potential drop is at least 100mV. While a greater potential drop

(contact resistance) can be achieved by further reducing the load, which will enable

higher temperatures to be achieved near the pin-disc interface; too light of a load will

result in small imprints whose diameter will become increasingly difficult to measure, as

discussed previously.

4.1.5 Comparison between Induction and Resistance Heating methods

Preliminary experimentation with induction and resistance heating methods revealed that for the same temperature set point (measured approximately 2 mm above the pin-disc interface), and the same duration of heating and rotation, the imprint diameter tended to be larger when resistance heating was used. As previously discussed in Section 3.3, the concentration of heat generation and relative thermal gradients for the two heating methods are notably different. Qualitatively, one might expect that the temperature at the pin-disc interface to be somewhat lower than that measured 2 mm above when using induction heating, since heat generation is concentrated within the bulk of the pin and flows down into the disc. Conversely, one might expect the interface temperature to be somewhat higher than that measured 2 mm above when using resistance heating; in so much as heat will be generated all throughout the pin, the cross-sectional area is smallest at the interface, so the rate of heat generation should be higher.

A mapping of peak temperature vs. resulting imprint diameter is shown in Figure 22 for both induction heating and resistance heating methods. Rather than using closed-loop temperature control, heating was performed under different constant power settings for varying lengths of time in order to achieve a range of peak temperatures. Testing was performed using uncoated WC pins loaded against flat, ground discs of Ti6Al4V under 500N of load. This disc material was selected on the basis that a collaborating graduate student, Hao Yu Li, was using this same material in FE modelling of the tribometer and had reliable Johnson Cook parameters available. Li ran his model under the same loading conditions, constraining the pin-disc interface temperature to fixed values and allowed
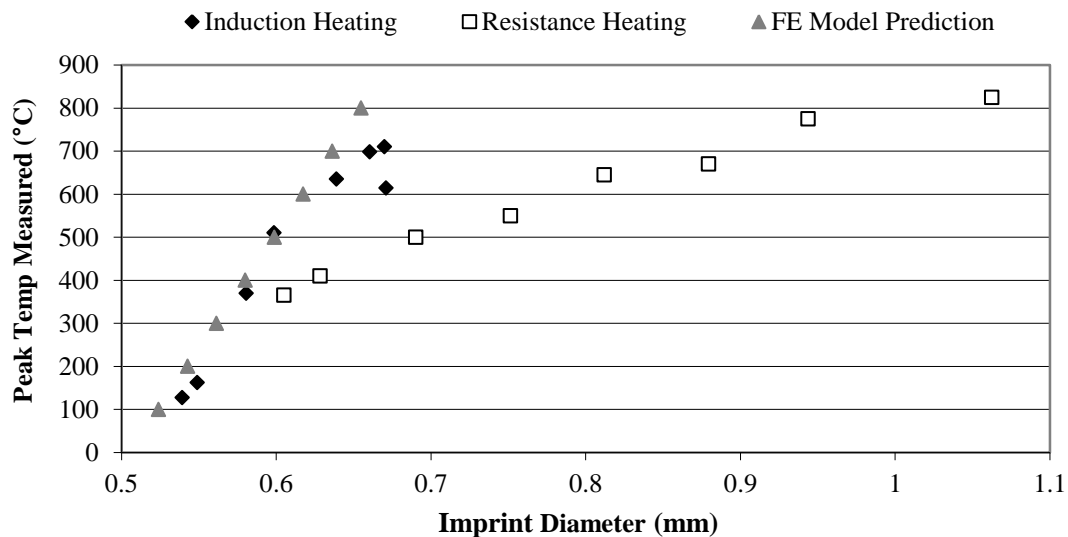
Figure 22: Mapping of Peak Temperature vs. Imprint Diameter

the simulation to run until thermal equilibrium within the disc was achieved. His results

of constrained interface temperature vs. resulting imprint diameter are also presented in

Figure 22 and follow closely with those results from the induction heating tests. Thus, the

temperature measured by the pyrometer 2mm above the interface more closely

corresponds to the real interface temperature when using induction heating than when

using resistance heating. This close similarity in temperatures was also observed by

Biksa, who inserted thermocouple probes into a preformed imprint prior to reloading the

pin and then activating the induction heater; he observed that the interfacial temperature

measured by the thermocouple was in good agreement with that measured by the infrared

pyrometer 2mm above the interface, exceeding it by no more than 5% (2010, pp. 140-

143). Unfortunately, the Johnson Cook parameters that Li had available to use were not

populated for temperatures in excess of 800°C; as such, sufficiently high interface

temperature simulations could not be run so as to generate imprint diameters as large as

some of those measured after high power resistance heating tests. It is thus probable that

the interfacial temperatures may be several hundred degrees higher than those measured 2mm above the interface, which would confirm the increased heat generating capability of the resistance welder over the induction heater. However, it remains an important step to determine how to accurately quantify the temperature at the pin-disc interface using the electrical resistance heating method given the complexity of interaction in this zone.

4.2 Soft Pin on Hard Disc Configuration

Some exploration was also conducted into specimen reversal, fabricating a pin out of the workpiece material and using a plain geometry cutting insert in the place of the disc. This configuration promises to be faster and overall cheaper to perform. The cost per uncoated carbide pin can easily range upward of 50 CAD and must be specially ordered, whereas a basic geometry cutting insert is typically in the range of 5 to 15 CAD and is available off the shelf with next day delivery in many cases. Furthermore, these cutting inserts can be purchased with a wide range of coatings already deposited, whereas the custom carbide pins would need to be sent out for coating, which adds time and another variable to control in the experiments. However, the contact mechanics are different from those in the hard pin on soft disc configuration, so it represents a deviation from testing recommended by Biksa as well as by Shuster. As such, a similar but not as exhaustive set of tests as with the hard pin on soft disc configuration in order to determine what input parameters should be used.

4.2.1 Influence of Normal Load on Contact Stress and COF

Whereas in hard pin on soft disc tests, a reasonably well defined spherical imprint is formed in the soft disc; in the case of soft pin and hard disc tests, plastic deformation occurs in the tip of the pin, resulting in a flat being formed. From experience, it was found difficult to measure the diameter of the flat under optical microscope for purely static tests. However after a few seconds of rotation, a reasonably well defined flat region on the pin tip can be distinguished, making measurements possible. Furthermore, traces of the contact area can also be observed on the insert in the form of transferred material.

TiAl6V4 pins of 1/4" diameter were loaded against flat WC uncoated inserts under various normal loads. The load was maintained for 60s prior to rotation at 1RPM for 5s. Values for load and torque were calculated using measured data from the last 0.5 seconds of rotation. Table 11 shows the variation of output parameters, including COF, with the load applied. Based on this limited testing the COF and shear stress tend to increase with normal load, as does increased flat imprint diameter and torque measurement.

Table 11: Variation in output parameters with applied normal load - soft pin on hard disc

Load	Torque (Nm)	Diameter (mm)	Normal Stress (MPa)	Shear Stress (MPa)	COF
500	0.026	0.603	1742	447	0.256
1000	0.069	0.816	1918	489	0.255
1500	0.142	0.966	2045	604	0.295
1900	0.232	1.103	1990	662	0.332

4.2.2 Influence of Reusing Pins and Rotational Time on COF

Inconel 718 pins (1/4" diameter) were tested against flat, uncoated WC inserts, as received. The pin was loaded against the insert to 1500 N and held stationary for 30 seconds, and then the insert was rotated at 1 RPM for 5 seconds. Multiple replicates of

this test were performed using the same pin, cleaning the tip with an alcohol wipe but not polishing. Thus the pin would have a pre-existing, strain-hardened flat instead of a polished, spherical tip for successive tests. This was an attempt to see the influence of rotation time on measured COF; as well, it would illustrate whether or not a new pin tip needs to be used for test replicates. A summary of reaction torque, imprint diameter, and calculated normal stress, shear stress and COF are presented in Table 12. It can be observed that with successive tests, the measured torque and imprint diameter grow larger. With a constant 1500 N load applied, the average normal stress is thus reduced with each test; combined with the increase in average shear stress, the COF is seen to grow considerably with each successive test. The actual recorded torque responses are presented in Figure 23, which highlights not only the increasing torque values recorded with successive tests, but also the changing characteristics of the torque response. For tests 1 and 2, the torque is at its maximum at the start and decays slightly throughout the 5 seconds of rotation. In tests 3 and 4, the torque response is essentially flat for the first second or so before gradually increasing. In tests 5 and 6, the initial torque response is characterized by a smooth edge before entering a zone of stable, linear growth.

With these results in mind, it is evident that new (or at least refurbished pin tips) must be used for each test to achieve repeatable results.

Table 12: Results from successive tests using the same Inconel pin against uncoated inserts

Test	Torque (Nm)	Diameter (mm)	Normal Stress (MPa)	Shear Stress (MPa)	COF
1	0.060	0.939	2170	278	0.128
2	0.104	0.956	2093	455	0.217
3	0.139	0.975	2007	573	0.286
4	0.165	0.999	1908	633	0.332
5	0.200	1.050	1734	661	0.381
6	0.251	1.099	1581	723	0.458
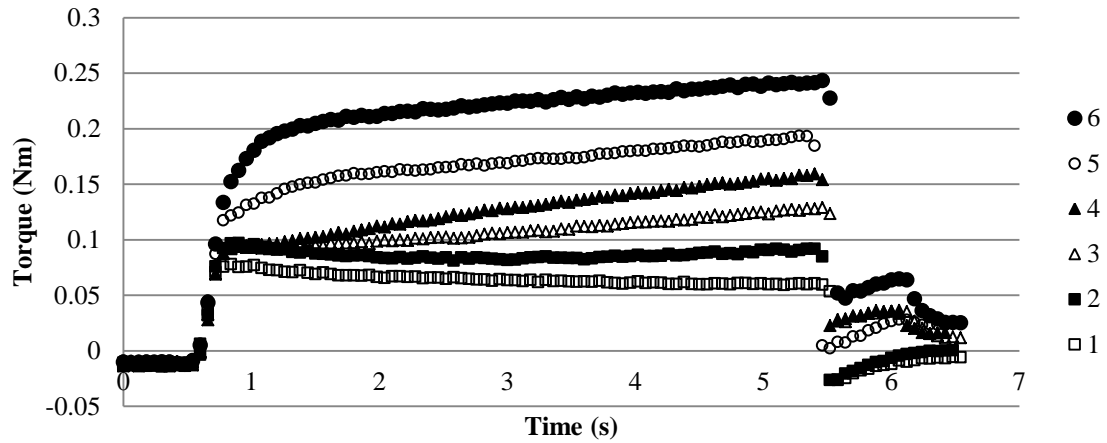
Figure 23: Torque response of successive tests using the same Inconel pin vs. WC inserts

Additional tests were performed at room temperature, under 500N and 1500N load, between Ti6Al4V pins and uncoated WC inserts. Loads were maintained for 30 seconds, and then the insert was rotated at 1RPM for 5s and 20s. Each test was repeated twice for a total of 8 tests, using a fresh pin tip each time. The variation in output parameters is presented in Table 13. Unfortunately, no clear trends can be discerned. Interestingly, the shear stress is bounded between roughly 600 to 750 MPa, irrespective of the load and rotation duration.

It is also striking to note the considerably higher shear stress and COF for those tests at 500N load and 5s rotation duration in these present tests than that recorded previously in Table 11 (447 MPa, 0.256). The only notable difference is the duration of the applied load prior to rotation (60s vs. 30s).

Table 13: Variation in output parameters with load and rotation time - soft pin on hard disc

Test	Torque (Nm)	Diameter (mm)	Normal Stress (MPa)	Shear Stress (MPa)	COF
500N, 5s (1)	0.039	0.614	1695	648	0.382
500N, 5s (2)	0.0.38	0.586	1862	722	0.387
500N, 20s (1)	0.038	0.578	1897	752	0.396
500N, 20s (2)	0.039	0.626	1626	608	0.374
1500N, 5s (1)	0.142	0.956	2092	622	0.297
1500N, 5s (2)	0.159	0.976	2034	653	0.321
1500N, 20s (1)	0.173	0.986	1964	691	0.352
1500N, 20s (2)	0.185	1.003	1901	702	0.369

4.3 Experimental Methodology Followed

The following outlines an experimental methodology that should be followed in conducting testing on the tribometer, based on the findings outlined earlier in Chapter 4 as well as other practical experience passed on by Biksa (2010).

1. Physical Installation of the Pin

Whereas WC-6Co pins are currently provided by a supplier, for soft pin on hard disc tests the pins are made of the workpiece material and must be fabricated in house. If possible, ¼" rod stock of the material should be ordered. The rod can be rough cut by hack saw into shorter segments of nominal length of 35 mm, which are then machined in a CNC Crown OKUMA lathe to put a ball tip on either end. Subsequently, these pin tips are polished by hand using successively finer grades of emery paper with a drop of oil as the pins are rotated in a drill press at about 800 RPM.

Next, the pin is inserted into the appropriately sized collet and tightened by two 9/16" wrenches. A generous amount of torque should be applied in order to ensure a tight grip and so achieve minimal electrical contact resistance between the various mating surfaces in the assembly. The assembly can then be installed in the adjustable 4-screw aluminum jig. The mounting flange of the collet assembly is held flush with the bottom face of the

jig and the four screws are gradually tightened with an alley key until the collet assembly is held in place. A dial indicator is mounted around the spindle and the probe is gently brought into contact with the pin close to its tip. The 4 screws are orthogonally oriented and can be tightened or loosened appropriately to allow the assembly to horizontally translate until the pin tip is radially aligned with the spindle to within 0.02mm.

2. Polishing of the Pin Tip

Particularly if the pin is coated, preliminary polishing of the pin tip should be performed to remove roughness associated with hard microdroplets adhering from the coating deposition process. Even if the pin is uncoated, preliminary polishing is advisable. A small section of a polishing pad can be cut out and glued onto a flat coupon. This polishing coupon is clamped into place on the aluminum platform with the four screw-adjustable arms and a small dab of 0.05 micron aluminum oxide polishing paste is applied to the polishing pad. The operator should check to ensure that the electrical jumper cables are disconnected from aluminum platform. The pin is then manually lowered into the soft polishing pad and manually controlled polishing is carried out under a load of 5N and a spindle speed of 500RPM for 5 minutes. Once polishing is complete, the pin is manually retracted, the coupon removed, and the pin tip carefully wiped cleaned with an alcohol wipe.

3. Application of Black Constant Emissivity Paint

In order to accurately measure and control temperature near the pin-disc interface, a spot of black constant emissivity paint should be carefully applied just above the curvature of the pin tip and allowed to dry for 1 hour.

4. Physical Preparation and Installation of the Disc

Discs of the workpiece material should be nominally 6.25mm thick. Cross sectional area can vary. Square discs, 10mm x 10mm, were prepared out of AISI 1045, while round, 25mm diameter discs were prepared out of Inconel 718 and TiAl6V4. If possible, discs should be manually polished to a mirror finish. It is advised that formerly polished specimens that have been in storage for a while be repolished prior to testing. Emery paper should be used to remove any burrs and high points along the edges of the disc.

For soft pin on hard disc testing, the disc is actually a cutting insert. No prep work is required as the manufacturer has taken steps to ensure a finely ground surface finish.

The disc is placed and clamped onto the aluminum platform in a similar manner to the polishing coupon. Tightening of the screws may tend to lift the disc ever so slightly, so it should be pressed down by hand once all four arms are fastened in place. An alcohol wipe should then be used to clean the surface of both the disc and the pin tip, and the surfaces subsequently blown dry using clean compressed air.

5. Setup of Heating Equipment

In the Tribometer GUI, all manual controls for the heating equipment (induction heater and/or DC welder) should be disengaged. The power supply of the appropriate heating equipment should be switched on (if not already on). If using induction heating, the induction heating coil should be carefully positioned around the pin, the pin being manually raised or lowered as required. Also, the chilled water pump should be switched on (if not already on). If using resistance heating, the jumper cables should be fastened to the four corners of the aluminum platform.

6. Other Physical Adjustments

The pin should be manually lowered until it is just above the surface of the disc. The position and orientation of the infrared pyrometer should be adjusted, if necessary, such that the red beams converge to a 1.5mm diameter spot just above the pin tip, over the area covered with the black constant emissivity paint. The valve of the vortex chiller should be fully opened, and the nozzle aimed at and positioned about 10mm from the nut of the collet assembly.

7. Selection and Verification of Testing Parameters

Within the Tribometer GUI, 'Prep & Run Test' mode should be selected and appropriate test parameters specified. From experience, it is advisable to set the duration of the *Preload*, *Heating*, and *Full Load* phases to be 30s, 5s, and 5s, respectively. Preload can also be set to be the same as full load. These recommended guidelines were followed for all experiments to be discussed later.

The programmed test sequence, as described in Chapter 3.4, is executed and the operator monitors the measured variables and the displayed stages of testing for any anomalies. If necessary, the testing can be aborted by pressing the E-stop hard button located on the tribometer or the 'STOP' button in the GUI.

8. Further Measurement and Analysis

Following a successful test, the user removes the disc from the platform and measures the diameter of the formed imprint using an optical microscope. In the case of soft pin on hard disc tests, the pin can be removed and the diameter of the resulting flat spot on the tip can be similarly measured for comparison with the diameter of the smeared print on

the hard disc. Despite fine measurement resolution (0.001mm), discerning the true edge of the imprint is difficult. Therefore, two measurements of diameter at orthogonal orientations should be taken, for a total of four measurements. These are averaged to give an estimate of the imprint diameter.

The saved data file is exported to Microsoft Excel and plots of the measured variables (specifically load, temperature, and torque) with respect to time are generated. The value of torque is taken to be the average of the last 0.5s of rotation referenced to an average of the torque signal over roughly 10s prior to rotation. This is due to the fact that the torque signature changes during the loading and unloading of the pin and is not zero at the onset of rotation.

9. Exceptions

In certain instances, deviations from the above procedure may be necessary. For instance, it was observed that during high temperature tests (750°C and above), only marginal stability of measured variables could be achieved in the automated test sequence – fluctuations in temperature corresponded to fluctuations in applied load, as well as reaction torque once rotation had begun. In an effort to overcome this and get steady torque data, a manual, user-prompted test sequence had to be applied. This involved the user counting the approximate time of various steps in the test sequence and manually triggering the start and stop of data logging, loading, heating, and spindle rotation. Closed-loop control of applied load and spindle speed were still used; however, control of temperature was regulated directly by the user, monitoring the temperature visually and adjusting the command signal sent to the welder manually from within the GUI.

Chapter 5. Tribometer Experiments and Correlations to Machining

Samples of various workpiece materials were prepared, either in disc or pin format. Some of these have been tested extensively, while others remain to be tested. What follows is a summary of testing performed on two different workpiece materials: AISI 4340 steel and AISI 1045 steel. Admittedly, the tests performed on AISI 4340 steel were performed much earlier than most of the 'preliminary' tests described previously. As such, the procedures used did not conform explicitly to those just described. However, these tests do highlight some of the promise in using the soft pin on hard disc configuration; as such, it is herein described.

5.1 AISI 4340 Steel

Pins were fabricated out of nominally 1/4" AISI 4340 steel rod that had been heat treated to HR 45. These pins were gripped in a 6.5 mm collet and loaded against triangular shaped grooving inserts coated with TiCN as well as TiCN + WS$_2$. An applied load of 500N was maintained throughout the duration of the test. Induction heating was used to heat the pin tip near the contacting interface to 400°C and 600°C. Once load and temperature had stabilized, the disc was rotated with respect to the pin at a constant speed of 4RPM for 30s. Due to the propensity of the pin tip to significantly deform under load, heating, and rotation, a new pin tip was used for each successive test.

The torque sensor response was generally shown to increase sharply at the start of rotation and then steadily rise throughout the duration of rotation, somewhat plateauing toward the end of the test. In some cases, the maximum torque was observed midway

through rotation, the torque signal decreasing toward the end. For the purposes of calculating COF using the aforementioned experimental equation, torque was calculated as the average of 2 seconds of torque data around the time of maximum torque minus the average of 2 seconds of torque data just prior to rotation commencing. Force was calculated as the average of the load cell signal throughout the duration of the full 30 seconds of rotation. Figure 24 presents the results of COF vs. Temperature for the two different coated inserts vs. AISI 4340 steel pins under the testing conditions specified. The error bars were calculated based on the standard deviation of two test replicates.

The coated insert with the WS_2 layer exhibited reduced COF at the tested temperatures. The results are quite distinct at 400°C; however, the error bars do overlap at 600°C. Sliney (1982) reports that under conventional pin-on-disc tribometer testing the COF for WS_2 increases dramatically between 400°C and 600°C, linking the increased COF to the increased rate of oxidation at higher temperatures.
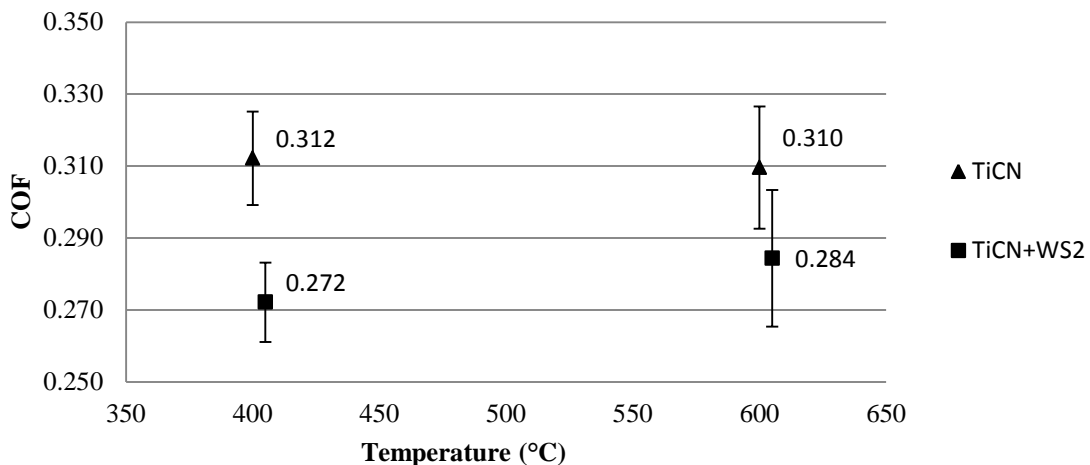

Figure 24: COF vs. Temperature results, induction heating, coated inserts vs. AISI 4340 pins

Based on these results the effectiveness of the WS_2 layer in reducing friction is largely

lost at 600°C, which could explain the overlap in error bars. Interestingly, this is within

the temperature range at which WS_2 begins to oxidize (Kustas, Fehrehnbacher &

Komanduri, 1997). Tool life improvement was observed to be 5 times at Linamar during

machining of a hardened structural steel similar to hardened 4340 (Fox-Rabinovich,

2012).

5.2 AISI 1045 Steel

Tests were performed using TiAlN-coated and uncoated WC pins against polished

discs made of AISI 1045 steel. A normal load of 500N was maintained for 30s, followed

by heating of the pin-disc interface to varying temperatures and then rotation of the disc

relative to the pin at a speed of 1RPM for 5s.

In order to achieve 750°C, the applied load had to be reduced to 250N – this enabled

sufficiently high contact resistance between the pin and disc. However, at such high

temperatures Cobalt was observed to diffuse out from the uncoated cemented carbide

pins, forming a blue-green Cobalt oxide layer on the exposed pin surface. Due to the

growth in the disc imprint area as interfacial heating occurs, let alone as the disc is

rotated, there is a real risk of Cobalt oxide forming on the outer regions of the pin tip

prior to these regions contacting the disc imprint. The resulting interface would then be

part cemented carbide and part Cobalt oxide against AISI 1045.

In order to help ensure that the interface area does not grow during heating, the pin

was first loaded up to 1000N against the disc for 60s and then the load reduced to 250N

prior to heating and rotation. This load was selected in order to produce an imprint of approximately the same size as that generated during the elevated temperature test under steady 250N load. Measurement of the imprint diameter after these modified tests revealed negligible growth in diameter. For consistency sake, this same high temperature procedure was used in testing the TiAlN coated pin against AISI 1045 discs.

Figure 25 shows the plot of COF vs. Temperature for the uncoated and TiAlN-coated WC pins against AISI 1045 steel discs. Particularly at elevated temperatures, the TiAlN coating results in notably lower COF than the uncoated WC.
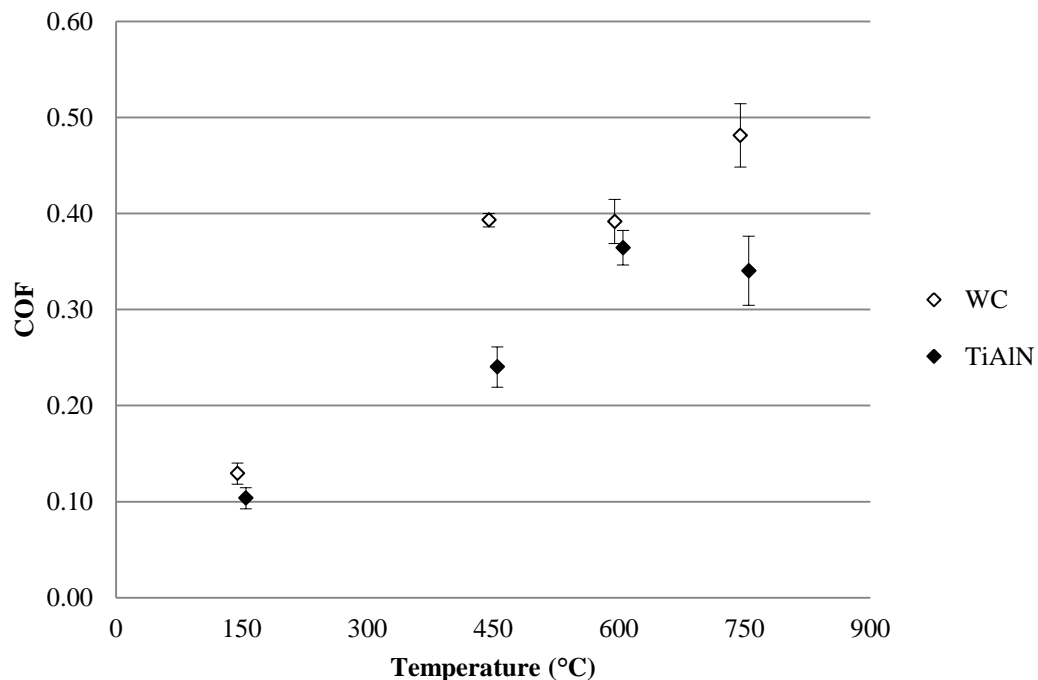
Figure 25: COF vs. Temperature results, resistance heating, hard pins vs. AISI 1045 discs

In order to relate these findings to actual machinability, in house turning tests were carried out on a Boehringer VCM180 lathe. A cylinder of AISI 1045 was turned using uncoated and TiAlN coated cemented carbide CNGG120408FS cutting inserts supplied

by Kennametal. Machining was performed without coolant at surface speeds of 100 and

400 m/min, maintaining a constant feed rate of 0.20 mm/rev and a constant depth of cut

of 0.25 mm. The inserts were held in a Signature Tool Inc. T60201 tool holder, which

was mounted in a 3-component Kistler 9121 Piezoelectric Tool Dynamometer in order to

obtain cutting force measurements. Flank wear measurements of the cutting inserts were

performed on a Mitutoyo TM optical microscope with crosshairs and a linear encoder

with 0.001 mm resolution.

   Figure 26 presents tool flank wear versus length of cut for the cutting tests. For a

given insert, tool life was notably longer at 100 m/min than at 400 m/min. At both cutting

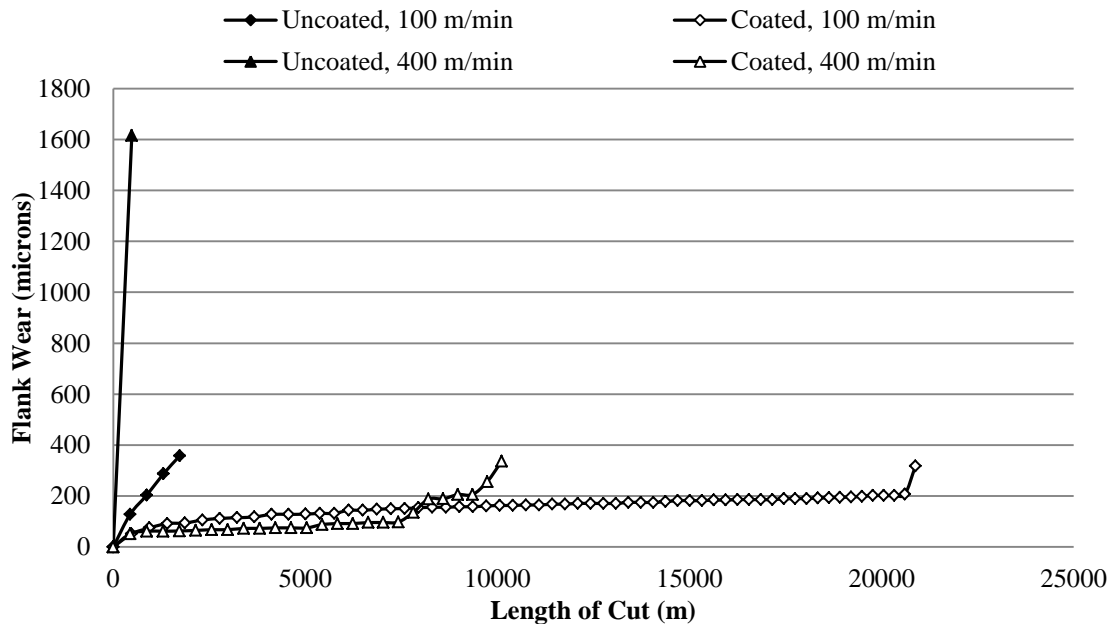speeds, the wear rate of the TiAlN coated insert was much lower.

Figure 26: Flank wear vs. Length of cut for dry turning of AISI 1045

Table 14 summarizes the forces acting on the tool during the cutting tests. The cutting

force, F_c, and thrust (feed) force, F_t, were obtained directly from the force sensor data;

whereas the friction force, F, and normal force, N, acting on the tool rake face were

calculated according to Equation 2.6. The exact rake angle was unknown, so calculations

were performed assuming a rake angle of 0° as well as 10° to exemplify the trends. This

is a preliminary analysis only, since Equation 2.6 assumes orthogonal cutting conditions

whereas this was a turning process with force components in three perpendicular

directions. Furthermore, edge-radius effects, which give rise to a ploughing component in

the tool force measurements, were not taken into consideration. Nonetheless, it is

interesting to note the reduction in all forces as well as the ratio F/N when cutting with

the coated insert. The drop in normal force, N, could reflect additional thermal softening

of the work material due to a higher tool-chip interface temperature owing to a lower

thermal conductivity of the coated tool. The drop in friction force, F, is small in

magnitude but significant in that it still leads to noticeable reduction in the ratio F/N,

despite the already discussed decrease in normal force, N.

Table 14: Analysis of tool forces from AISI 1045 cutting tests

Speed [m/min]	Tool	Fc [N]	Ft [N]	0° rake assumed			10° rake assumed		
				F [N]	N [N]	F/N	F [N]	N [N]	F/N
100	Uncoated	222	116	116	222	0.52	153	239	0.64
	Coated	192	81	81	192	0.42	113	203	0.56
400	Uncoated	133	39	39	133	0.29	62	138	0.45
	Coated	123	30	30	123	0.24	51	126	0.40

Overall, this analysis of the tool forces suggests that friction at the tool-chip interface is reduced for the coated insert, in agreement with the friction coefficient measurements obtained from the tribometer. This reduction in friction corresponds directly with the increase in tool life of the coated tool in terms of flank wear.

However, other tool wear forms and undesirable phenomena were qualitatively observed in addition to flank wear. As noted earlier, a crater on the rake face of the tool is typically the result of diffusion, a mechanism which can also contribute to flank wear. Sizeable crater wear was noted on the uncoated carbide inserts but much less so on the TiAlN-coated inserts. While a formal investigation via Scanning Electron Microscopy on the underlying mechanisms of flank wear on the tools was not carried out, it is postulated that decreased diffusion at the rake face would be accompanied by decreased diffusion at the flank face. Thus the ability of the TiAlN coating to function as a diffusion barrier may contribute to its improved tool life as measured by flank wear.

Chapter 6. Conclusions

Several modifications were made to the tribometer developed by Biksa to increase the overall functionality of the system. In particular, a DC welding power supply capable of 200A current output was purchased and integrated into the setup; modifications were made to the load column in order to facilitate safe and easy connection of welding cables, installation and alignment of the pin relative to the spindle, and electrical isolation of sensors and electronics. As well, an entirely new Graphical User Interface was developed in Labview to handle control of all components as well as measurement of important variables.

Extensive experimentation was performed on the reconfigured tribometer in order to explore the sensitivity of output parameters to different input parameters. Key findings from these preliminary tests include:

- Under applied loads ranging from 125 to 2000 N, the achievable mean normal contact stress tends to range between 2 to 4 times the workpiece material's yield strength.

- A smaller imprint diameter (resulting from a lighter load or increased hardness of disc material) has a greater measurement uncertainty.

- Heavier loads trigger increased friction and stiction in the lead screws and result in less precise control and hence greater uncertainty in the load.

- Lighter loads enable higher interface temperatures and thermal gradients more representative of machining when resistance heating is used.

- For the same measured temperature 2 mm above the interface, resistance heating leads to substantially larger imprints than induction heating. Based on FE simulations performed by Li, infrared pyrometer measurements of temperature 2mm above the interface when using with the induction heater are much more representative of those at the real interface than when using the resistance heating method. The interface temperature could be several hundred degrees higher than that measured during resistance heating, and the heat input into the disc is expected to be significantly greater.

- The imprint diameter and torque tend to grow with rotation time; under constant load, the mean normal contact thus decreases; however, the apparent shear stress increases, for reasons that are still not entirely clear. Thus, the calculated COF will depend on rotation time, and shows greater repeatability for shorter rotation durations.

- Coated pins need to be polished prior to testing; failure to do so will likely result in substantially higher COF readings due to the roughness associated with hardened microdroplets of coating material on the surface.

- For the soft pin on hard disc configuration, successive tests using the same pin tip led to increasing torque measurements and COF calculations; as such, a new pin tip should be used for each test to be performed.

- Unfortunately, the effect of contact load and rotation time on COF for the soft pin on hard disc configuration is somewhat unclear; in general, a greater variation in COF calculation has been noted using this approach.

Following these preliminary tests, complete sets of experiments were performed using uncoated and coated WC pins loaded against AISI 1045 steel. Testing involved loads of 500N held for 30s, followed by heating to the temperature set point, followed by 5s of rotation at 1RPM. The COF was observed to be lower for the TiAlN-coated pin as compared with the uncoated pin, over a range of temperatures up to 750°C. The lower COF was observed to correlate well with the improved tool-life of TiAlN at different cutting speeds as well as lower cutting forces, notably a lower friction force acting on the tool rake face.

Chapter 7. Future Work and Recommendations

Critical to the success of the physics-based framework of coating design in the MMRI is accurate and repeatable friction measurements on the tribometer. The following are suggestions of work and investigations that should be carried out to move the project towards further success:

1) Cleanliness of the pin and disc is paramount to obtaining repeatable measurements. Biksa suggested investigating the use of ultrasonic cleaning prior to testing. Removal of the pin from the tribometer to perform ultrasonic cleaning in between tests, however, would likely be cumbersome, unduly time-consuming, and introduce subtle changes into the alignment of the pin. Devising a method to perform such cleaning of the pin on the tribometer itself may be a feasible solution.

2) A means of more reliable temperature measurement at the pin-disc interface when using electrical resistance heating methods. One possibility would be to hold an isolated thermocouple adjacent to the interface during heating and observe how its measured output compares with that of the infrared pyrometer.

3) Testing should be conducted using coatings of well-established frictional extremes (known lubricious and non-lubricious coatings) in order to assess the tribometer's ability to distinguish them.

4) Further investigate the closed-loop temperature control method in contrast to constant power heating in order to ensure temperature stability at elevated temperatures. However, constant power heating must be accompanied by

eliminating a host of other variables that would influence the temperatures

reached; this includes the electrical resistance at the collet nut; the length of the

pin extending from the collet to the disc; and the location, flow rate and

temperature of the chilled air nozzle system.

5) COF results generated to date should be validated in FE simulations. It would be

advisable to start with results of AISI 1045 against WC-6Co.

References

American National Standard (1985). *Tool Life Testing With Single-Point Turning Tools* (ANSI/ASME B94.55M-1985). New York: ASME.

Bailey, J. A. (1975). Friction in metal machining – mechanical aspects. *Wear*, *31*, 243-275.

Ben Abdelali, H., Claudin, C., Rech, J., Ben Salem, W., Kapsa, Ph., & Dogui, A. (2012). Experimental characterization of friction coefficient at the tool-chip-workpiece interface during dry machining of AISI 1045. *Wear*, *286-287*, 108-115.

Biksa, A. (2010). *Tribological Characterization of Surface Engineered Tooling*. (Master's Dissertation). McMaster University, Hamilton, ON, Canada.

Bonnet, C., Valiorgue, F., Rech, J., Claudin, C., Hamdi, H., Bergheau, J. M., & Giles, P. (2008). Identification of a friction model – Application to the context of dry cutting of an AISI 316L austenitic stainless steel with a TiN coated carbide tool. *International Journal of Machine Tools & Manufacture*, *48*, 1211-1223.

Claudin, C., Mondelin, A., Rech, J., & Fromentin, G. (2010). Effects of straight oil on friction at the tool-workmaterial interface in machining. *International Journal of Machine Tools and Manufacture, 50*, 681-688.

Dorward, R.C. & Bouvier, C. (1998). A rationalization of factors affecting the strength, ductility and toughness of AA6061-type Al-Mg-Si-(Cu) alloys. *Materials Science and Engineering : A*, *254*(1-2), 33-44.

Ezugwu, E.O., Bonney, J., Fadare, D.A. & Sales, W.F. (2005). Machining of nickel-base, Inconel 718, alloy with ceramic tools under finishing conditions with various coolant supply pressures. *Journal of Materials Processing Technology*, *162-163*, 609-614.

Filice, L., Micari, F, Rizzuti, S. & Umbrello, D. (2007). A critical analysis on the friction modelling in orthogonal machining. *International Journal of Machine Tools & Manufacture*, *47*, 709-714.

Fox-Rabinovich, G.S., Yamamoto, K., Aguirre, M.H., Cahill, D.G., Veldhuis, S.C., Biksa, A., Dosbaeva, G. & Shuster, L.S. (2010). Multi-functional nano-multilayered AlTiN/Cu PVD coating for machining of Inconel 718 superalloy. *Surface & Coatings Technology*, *204*, 2465-2471.

Fox-Rabinovich, G.S., interview by Jeremy Boyd. *Discussions on tribology and tool wear* (2012).

Klocke, F. & Kriege, T. (1999). Coated tools for metal cutting – features and applications. *Annals of the CIRP*, *48*(2), 515-525.

Kustas, F. M., Fehrehnbacher, L. L. & Komanduri, R. (1997). Nanocoatings on cutting tools for dry machining. *Annals of the CIRP*, *46*(1), 39-42.

Merchant, M. E. (1945). Mechanics of the metal cutting process. I. Orthogonal cutting and a type 2 chip. *Journal of Applied Physics*, *16*(5), 267-275.

Rack, H.J. & Qazi, J.I. (2006). Titanium alloys for biomedical applications. *Materials Science and Engineering: C*, *26*(8), 1269-1277.

Rech, J., Claudin, C., & D'Eramo, E. (2009). Identification of a friction model – Application to the context of dry cutting of AISI 1045 annealed steel with a TiN-coated carbine tool. *Tribology International*, *42*, 738-744.

Sandvik Coromant. (1996). Modern Metal Cutting. New Jersey: Sandvik Coromant.

Shaw, M. C., Ber, A., & Mamin, P. (1960). Friction characteristics of sliding surfaces undergoing subsurface plastic flow. *Journal of Basic Engineering*, *82*, 342-346

Shaw, M. C. (1984). *Metal cutting principles*. New York: Oxford University Press Inc.

Sheikh-Ahmad, J.Y. & Bailey, J.A. (1999). The wear characteristics of some cemented tungsten carbides in machining particleboard. *Wear*, *225-229*, 256-266.

Sliney, H.E. (1982). Solid lubricant materials for high temperatures – a review. *Tribology International*, *15*(5), 303-315.

Tata Steel International. Engineering Steels – Medium Tensile Steel – AISI 1045. Retrieved from: http://www.tatasteelnz.com/downloads/MeduimTens_AISI1045.pdf

Trent, E. (1988a). Metal cutting and the tribology of seizure: I Seizure in metal cutting. *Wear*, *128*, 29-45.

Trent, E. (1988b). Metal cutting and the tribology of seizure: II Movement of work material over the tool in metal cutting. *Wear*, *128*, 47-64.

Trent, E. (1988c). Metal cutting and the tribology of seizure: III Temperatures in metal cutting. *Wear*, *128*, 65-81.

Trent, E.M & Wright, P.K. (2000). *Metal Cutting* (4th ed.). Boston, MA: Butterworth-Heinemann.

Whittle, D.P. & Stringer, J. (1980). Improvements in high temperature oxidation resistance by additions of reactive elements or oxide dispersions. *Philosophical*

Transactions of the Royal Society of London. Series A, Mathematical and Physical Sciences, *295*, 309-329.

Wu, P., interview by Jeremy Boyd. *Influence of von Mises stress on imprint diameter growth in MMRI tribometer simulations* (2011).

Zemzemi, F., Bensalem, W., Rech, J., Dogui, A., & Kapsa, P. (2008). New tribometer designed for the characterisation of the friction properties at the tool/chip/workpiece interfaces in machining. *Tribotest*, *14*, 11-25.

Zemzemi, F., Rech, J., Ben Salem, W., Dogui, A., & Kapsa, P. (2008). Identification of a friction model at tool/chip/workpiece interfaces in dry machining of AISI 4142 treated steels. *Journal of Materials Processing Technology*, *209*, 3978-3990.
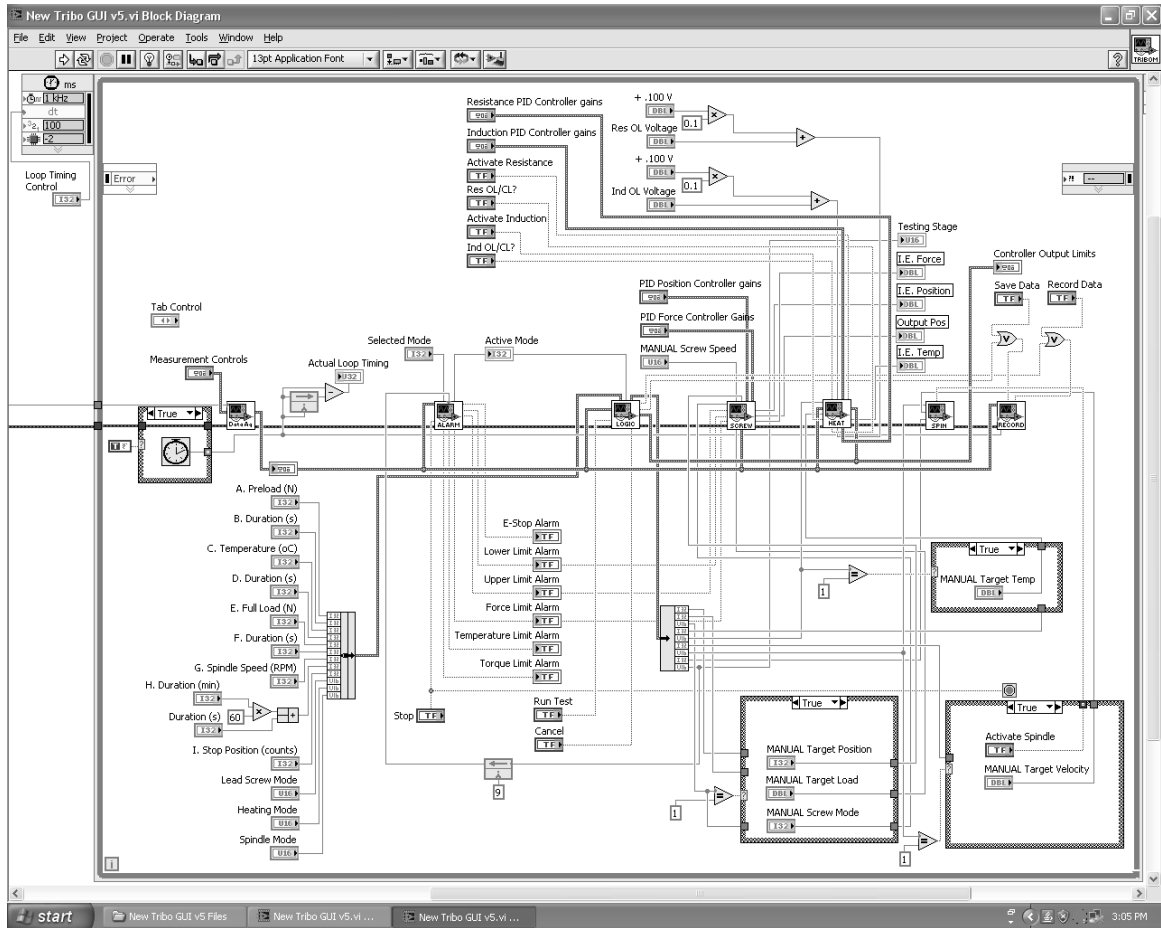
Appendix. Block Diagram of Tribometer Graphical User Interface

Figure 27: Block diagram of tribometer Graphical User Interface